

Next-Generation Quantum Theory of Atoms in Molecules for the Ground and Excited State of the Ring-Opening of Cyclohexadiene (CHD)

Tian Tian¹, Tianlv Xu¹, Steven R. Kirk^{1*}, Michael Filatov^{1,2} and Samantha Jenkins^{1*}

¹*Key Laboratory of Chemical Biology and Traditional Chinese Medicine Research and Key Laboratory of Resource Fine-Processing and Advanced Materials of Hunan Province of MOE, College of Chemistry and Chemical Engineering, Hunan Normal University, Changsha, Hunan 410081, China*

²*Department of Chemistry, Ulsan National Institute of Science and Technology (UNIST), 50 UNIST-gil, Ulsan 44919, Korea*

email: steven.kirk@cantab.net

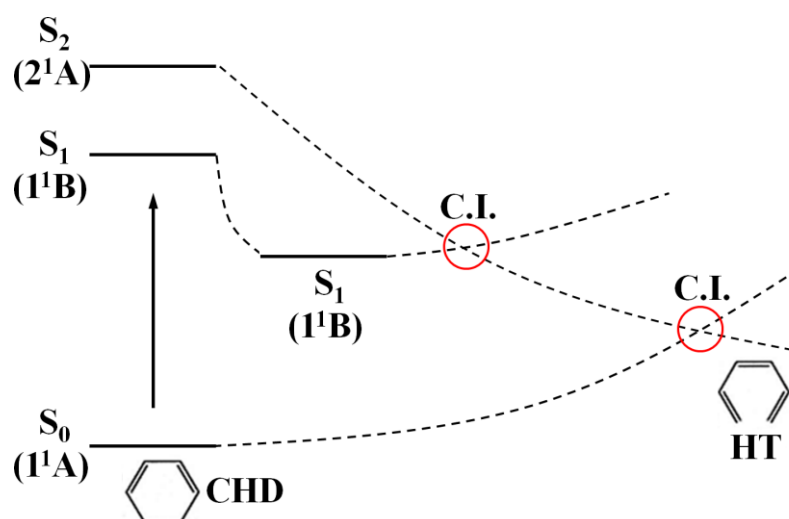
email: mike.filatov@gmail.com

email: samanthajsuman@gmail.com

The factors underlying the experimentally observed branching ratio (70:30) of the (1,3-cyclohexadiene) CHD→HT (1,3,5-hexatriene) photochemical ring-opening reaction are investigated. The ring-opening reaction path is optimized by a high-level multi-reference DFT method and the density along the path is analyzed by the QTAIM and stress tensor methods. The performed density analysis suggests that, in both S_1 and S_0 electronic states, there exists an attractive interaction between the ends of the fissile σ -bond of CHD that steers the ring-opening reaction predominantly in the direction of restoration of the ring. It is suggested that opening of the ring and formation of the reaction product (HT) can only be achieved when there is a sufficient persistent nuclear momentum in the direction of stretching of the fissile bond. As this orientation of the nuclear momentum vector can be expected relatively rare during the dynamics, this explains the observed low quantum yield of the ring-opening reaction.

Introduction

The photochemical electrocyclic ring-opening reaction of 1,3-cyclohexadiene (CHD) to 1,3,5-hexatriene (HT) is a prototypical reaction relevant for many photochemical ring-opening processes important for synthetic organic chemistry and biochemistry¹⁻⁵. The mechanism of this reaction was extensively studied by both experimental spectroscopic techniques^{1,6} and theoretical modeling^{2-5,7-10}. According to the widely accepted mechanism of this reaction^{1,3-5}, the photoexcitation (a $\pi \rightarrow \pi^*$ transition) at the ground electronic state (S_0) equilibrium geometry brings the molecule to the first excited electronic state (S_1) (1^1B state in the C_2 symmetry; the symmetry labels represent diabatic states), whereupon the nuclear wave-packet slides down the steep slope on the S_1 PES and the state's character changes from 1^1B to 2^1A (a $\pi \rightarrow \sigma^*$ transition). After that, the nuclear wave-packet continues to move on the S_1 PES and reaches an S_1/S_0 conical intersection (CI), where it switches to the S_0 state. Having switched to the S_0 state, the nuclear wave-packet splits into two branches, one traveling back to CHD and another propagating forward to HT. The latest gas phase experimental measurements yield 70:30 CHD:HT branching ratio⁶, which is generally consistent with 60:40 ratio for the reaction in solution¹¹.

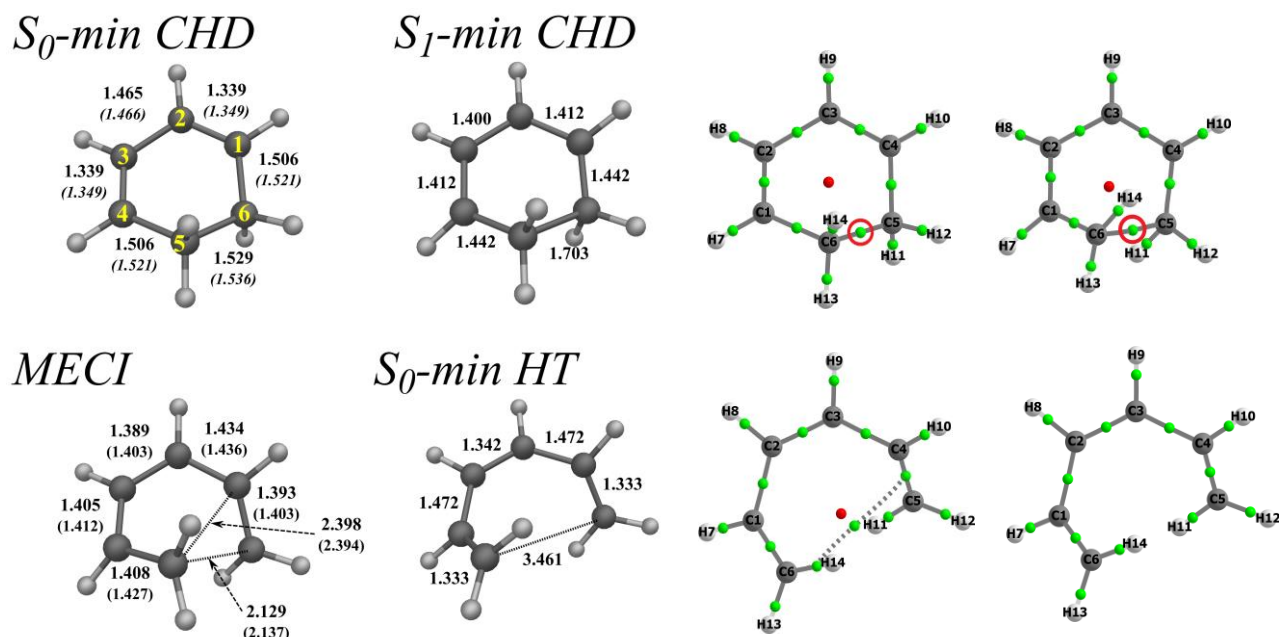


Scheme 1. Scheme of photochemical ring-opening reaction of CHD.

On the basis of CASSCF (and similar) calculations²⁻⁵ it was concluded that upon the $S_1 \rightarrow S_0$ non-adiabatic population transfer through this conical intersection the wave-packet splits into two branches already on the S_0 surface. A 50:50 CHD:HT branching ratio was deduced on the basis of these calculations and quantum dynamics simulations on fitted PESs^{2,7-9}. Early theoretical analysis of the CHD ring-opening reaction was heavily dominated by the CASSCF calculations, which predicted for the S_1/S_0 C.I. of CHD a bicyclic structure where the fissile C5-C6 bond and a bond with a neighboring atom form a nearly isosceles triangle^{3-5,12}.

The CASSCF calculations however, neglect the dynamic electron correlation, which has dramatic effect for the geometry of the S_1/S_0 conical intersection. The MSPT2 calculations resulted in a monocyclic geometry

of the S_1/S_0 C.I.¹². The subsequent TSH/MSPT2 NAMD simulations¹⁰ yielded branching ratio (60:40) in a better agreement with the experiment.



Scheme 2. Geometries of the ground S_0 and excited S_1 state minima and the S_1/S_0 MECI of CHD are shown in the left panel (gray scale). The values in parentheses show the experimental bond-lengths (italics) and bond-lengths obtained with the MSPT2 method (normal font) in Ref. 5. The corresponding molecular graphs (in color) for the CHD (FC-closed), CHD (C.I.) temporary state and HT (FC-open) configurations are shown in the right panel; with the ring-opening C5-C6 BCP being indicated by a red circle. Note, the C1-C5 bond in the grey-scale sketches corresponds to the C4---C6 BCP of the molecular graph. The undecorated red and green spheres indicate the positions of the ring critical points (RCPs) and bond critical points (BCPs) respectively.

Hence, a reasonable question to ask is what defines the CHD→HT photoreaction branching ratio? Are there electronic factors defining it, e.g., attractive bonding in the fissile C5-C6 bond, see **Scheme 2**, at the S_1/S_0 C.I., or is the branching ratio defined by purely dynamic factors, e.g., the momentum along the fissile C5-C6 bond?

To address these questions we have undertaken quantum chemical calculation of the minimum energy paths on the S_1 and S_0 PESs of the CHD ring-opening reaction. The computational method used in this work included the dynamic correlation from the outset; hence, predicting the correct S_1/S_0 C.I. with monocyclic geometry.

In this work, we shall investigate the ring-opening of the CHD along the MEPs in the S_0 and S_1 electronic states and analyze the resultant wave-functions with next-generation QTAIM that includes the bond-path framework set $\mathbb{B} = \{p, q, r\}$, see **Scheme 3**. Recently, the bond-path framework set \mathbb{B} was used to investigate the S_0 and S_1 electronic states of fulvene¹³. The bond-path framework set $\mathbb{B} = \{p, q, r\}$ is constructed using the ellipticity ε as a scaling factor and comprises three paths associated with the least p and most q preferred directions of accumulation and the bond-path r . The ellipticity ε , was chosen as a scaling factor for \mathbb{B} because it has already been found capable of differentiating between the S_0 and S_1 electronic states¹³. We

will use next-generation QTAIM to attempt to investigate mechanism involved in the CHD:HT branching ratio.

2. Theory and Methods

2.1 The QTAIM and stress tensor BCP properties; ellipticity ε , total local energy density $H(\mathbf{r}_b)$ and the stress tensor eigenvalue $\lambda_{3\sigma}$

We use QTAIM and the stress tensor analysis that utilizes higher derivatives of $\rho(\mathbf{r}_b)$ in effect, acting as a ‘magnifying lens’ on the $\rho(\mathbf{r}_b)$ derived properties of the wave-function. We will use QTAIM¹⁴ to identify critical points in the total electronic charge density distribution $\rho(\mathbf{r})$ by analyzing the gradient vector field $\nabla\rho(\mathbf{r})$. These critical points can further be divided into four types of topologically stable critical points according to the set of ordered eigenvalues $\lambda_1 < \lambda_2 < \lambda_3$, with corresponding eigenvectors \mathbf{e}_1 , \mathbf{e}_2 , \mathbf{e}_3 of the Hessian matrix. In the limit that the forces on the nuclei become vanishingly small, an atomic interaction line¹⁵ becomes a bond-path, although not necessarily a chemical bond¹⁶. The complete set of critical points together with the bond-paths of a molecule or cluster is referred to as the molecular graph.

In this investigation we have the closed-shell C5--C6 *BCP* and shared-shell C5-C6 *BCP* that comprise the CHD molecule, see **Scheme 2**. The bond notations “--“ and “-“ are used to distinguish instances where the Laplacian $\nabla^2\rho(\mathbf{r}) > 0$ for the closed-shell *BCPs* and $\nabla^2\rho(\mathbf{r}) < 0$ for shared-shell *BCPs*. Closed-shell *BCPs* may be divided into two categories: the strongest and weakest denoted by “--“ and “---“ corresponding to values of the total local energy density $H(\mathbf{r}_b) < 0$ and $H(\mathbf{r}_b) > 0$ respectively, see equation (1). We include in this investigation an example of the weakest category of bond; the closed-shell C4---C6 *BCP* that corresponds to the C1-C5 bond in **Scheme 2**.

The least and most preferred directions of electron accumulation correspond to the \mathbf{e}_1 and \mathbf{e}_2 eigenvectors respectively¹⁷⁻¹⁹ where the \mathbf{e}_3 eigenvector with associated eigenvalue λ_3 , indicates the direction of the bond-path at the *BCP*. The ellipticity $\varepsilon = |\lambda_1|/|\lambda_2| - 1$, where λ_1 and λ_2 are the negative eigenvalues with corresponding eigenvectors \mathbf{e}_1 and \mathbf{e}_2 respectively that provide the relative accumulation of $\rho(\mathbf{r}_b)$ in the two directions perpendicular to the bond-path. Recently, for the 11-cis retinal subjected to a torsion $\pm\theta$, we demonstrated that the \mathbf{e}_2 eigenvector of the torsional *BCP* corresponded to the preferred $+\theta$ direction of rotation as defined by the PES profile²⁰.

The stress tensor eigenvalue $\lambda_{3\sigma}$ is also associated with the bond-path and previously values of $\lambda_{3\sigma} < 0$ were found to be associated with transition-type behavior in biphenyl²¹ and molecular motors²² and indicated the bond critical point was close to rupturing and therefore we described as being *unstable*.

The total local energy density $H(\mathbf{r}_b)$ ^{23,24} is defined as:

$$H(\mathbf{r}_b) = G(\mathbf{r}_b) + V(\mathbf{r}_b), \quad (1)$$

where $G(\mathbf{r}_b)$ and $V(\mathbf{r}_b)$ are the local kinetic and potential energy densities at a *BCP*, defines a degree of covalent character: values of $H(\mathbf{r}_b) < 0$ for the closed-shell interaction, $\nabla^2\rho(\mathbf{r}_b) > 0$, indicates a *BCP* with a degree of covalent character and conversely a positive $H(\mathbf{r}_b) > 0$ reveals a lack of covalent character for the closed-shell *BCP*. A shared-shell *BCP* always possesses both $\nabla^2\rho(\mathbf{r}_b) < 0$ and $H(\mathbf{r}_b) < 0$ corresponding to short strong bonds e.g. C-C and C-H bonds.

2.2 The *QTAIM*, bond-path framework set $\mathbb{B} = \{p, q, r\}$

The bond-path length (BPL) is defined as the length of the path traced out by the $\underline{\mathbf{e}}_3$ eigenvector of the Hessian of the total charge density $\rho(\mathbf{r})$, passing through the *BCP*, along which $\rho(\mathbf{r})$ is locally maximal with respect to any neighboring paths. The bond-path curvature separating two bonded nuclei is defined as the dimensionless ratio:

$$(\text{BPL} - \text{GBL})/\text{GBL}, \quad (2)$$

Where the BPL is the associated bond-path length and the geometric bond length GBL is the inter-nuclear separation. The BPL often exceeds the GBL particularly for weak or strained bonds and unusual bonding environments²⁵. For 3-D bond-paths, there are minor and major radii of curvature specified by the directions of $\underline{\mathbf{e}}_2$ and $\underline{\mathbf{e}}_1$ respectively.²⁶ In this investigation we suggest the involvement of the $\underline{\mathbf{e}}_3$ eigenvector also, in the form of a bond-path twist because earlier it was observed during calculations of the $\underline{\mathbf{e}}_1$ and $\underline{\mathbf{e}}_2$ eigenvectors at successive points along the bond-path that in some cases, these eigenvectors, both being perpendicular to the bond-path tracing eigenvector $\underline{\mathbf{e}}_3$, 'switched places'. We recently observed that the calculation of the vector tip path following the unscaled $\underline{\mathbf{e}}_1$ eigenvector would then show a large 'jump' as it swapped directions with the corresponding $\underline{\mathbf{e}}_2$ eigenvector¹³. This phenomenon indicated a location where the ellipticity $\varepsilon = 0$ due to degeneracies in the corresponding λ_1 and λ_2 eigenvalues, see the **Supplementary Materials S4** for a discussion on the choice of the ellipticity ε as the scaling factor.

With n scaled eigenvector $\underline{\mathbf{e}}_2$ tip path points on the q -path where $\varepsilon_i =$ ellipticity at the i^{th} bond-path point \mathbf{r}_i on the bond-path \mathbf{r} . It should be noted that the bond-path \mathbf{r} is associated with the λ_3 eigenvalues of the $\underline{\mathbf{e}}_3$ eigenvector does not take into account differences in the λ_1 and λ_2 eigenvalues of the $\underline{\mathbf{e}}_1$ and $\underline{\mathbf{e}}_2$ eigenvectors. Analogously, for the $\underline{\mathbf{e}}_1$ tip path points we on the p -path where $\varepsilon_i =$ ellipticity at the i^{th} bond-path point \mathbf{r}_i on the bond-path \mathbf{r} , where the p_i and q_i are defined by:

$$p_i = \mathbf{r}_i + \varepsilon_i \underline{\mathbf{e}}_{1,i} \quad (3a)$$

$$q_i = \mathbf{r}_i + \varepsilon_i \underline{\mathbf{e}}_{2,i} \quad (3b)$$

We referred to the next-generation QTAIM interpretation of the chemical bond as the *bond-path framework set*, denoted by \mathbb{B} , where $\mathbb{B} = \{p, q, r\}$ with the consequence that for the ground state a bond is comprised of three ‘linkages’; *p*-, *q*- and *r*-paths associated with the \underline{e}_1 , \underline{e}_2 and \underline{e}_3 eigenvectors, respectively.

The *p* and *q* parameters define eigenvector-following paths with lengths \mathbb{H}^* and \mathbb{H} , see **Scheme 2**:

$$\mathbb{H}^* = \sum_{i=1}^{n-1} |\mathbf{p}_{i+1} - \mathbf{p}_i| \quad (4a)$$

$$\mathbb{H} = \sum_{i=1}^{n-1} |\mathbf{q}_{i+1} - \mathbf{q}_i| \quad (4b)$$

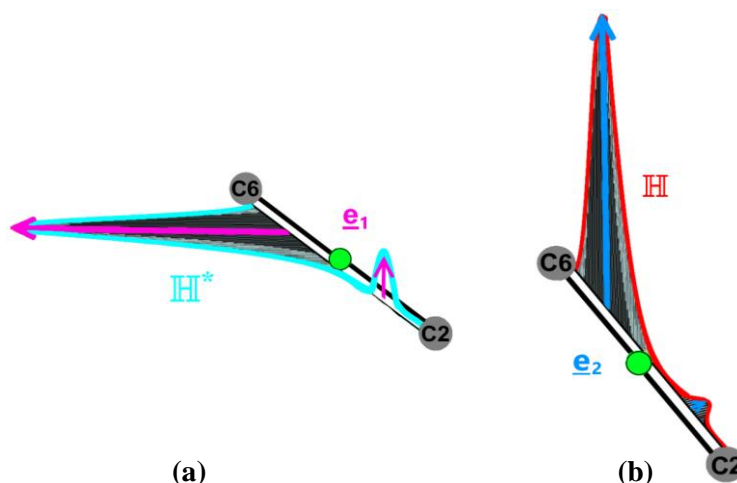
The lengths of the *eigenvector-following paths* \mathbb{H}^* or \mathbb{H} refers to the fact that the tips of the scaled \underline{e}_1 or \underline{e}_2 eigenvectors sweep out along the extent of the bond-path, defined by the \underline{e}_3 eigenvector, between two bonded nuclei connected by a bond-path. In the limit of vanishing ellipticity $\varepsilon = 0$, for all steps *i* along the bond-path then $\mathbb{H} = \text{BPL}$.

From equation (3a) and equation (3b) we see for shared-shell BCPs, in the limit of the ellipticity $\varepsilon \approx 0$ i.e. corresponding to single bonds, we then have $\mathbf{p}_i = \mathbf{q}_i = \mathbf{r}_i$ and therefore the value of the lengths \mathbb{H}^* and \mathbb{H} attain their lowest limit; the bond-path length (*r*) BPL. Conversely, higher values of the ellipticity ε , for instance, corresponding to double bonds will always result in values of \mathbb{H}^* and $\mathbb{H} > \text{BPL}$. Discussion on the uniqueness of the \mathbb{H}^* and \mathbb{H} is provided in the **Supplementary Materials S4**.

Analogous to the bond-path curvature, see equation (2), we may define dimensionless, *fractional* versions of the eigenvector-following path with length \mathbb{H} where several forms are possible and not limited to the following:

$$\mathbb{H}_f = (\mathbb{H} - \text{BPL})/\text{BPL} \quad (5)$$

A similar expressions to equation (5) for \mathbb{H}_f^* can be derived using the \underline{e}_1 eigenvector.



Scheme 3. The pale-blue line in sub-figure (a) represents the path, referred to as the eigenvector-following path with length \mathbb{H}^* , swept out by the tips of the scaled \underline{e}_1 eigenvectors, shown in magenta, defined by equation (4a). The red

path in sub-figure (b) corresponds to \mathbb{H} , constructed from the path swept out by the tips of the scaled \mathbf{e}_2 eigenvectors, shown in mid-blue and is defined by equation (4b). The pale-blue and mid-blue arrows representing the \mathbf{e}_1 and \mathbf{e}_2 eigenvectors are scaled by the ellipticity ε respectively, where the vertical scales are exaggerated for visualization purposes. The green sphere indicates the position of a given *BCP*. Details of how to implement the calculation of the \mathbb{H}^* and \mathbb{H} are provided in the **Supplementary Materials S4**.

Previously, we considered the S_0 and S_1 electronic states of fulvene for the bond-path framework set $\mathbb{B} = \{(\mathbf{p}_0, \mathbf{p}_1), (\mathbf{q}_0, \mathbf{q}_1), \mathbf{r}\}^{13}$.

3. Computational Details

The potential energy surfaces of the S_1 and S_0 states of CHD along the ring-opening reaction coordinate were investigated using the state-interaction state-averaged REKS (SI-SA-REKS or SSR, for brevity) method²⁷. The SSR method employs ensemble density functional theory to describe the non-dynamic electron correlation occurring due to multi-reference character of the S_0 state and to obtain excitation energies from a variational time-independent formalism. By contrast to the popular state-averaged CASSCF (SA-CASSCF) methodology, the SSR method includes the dynamic electron correlation from the outset; thus providing very accurate description of the PESs of the S_1 and S_0 states and conical intersections between the states^{28,29}.

In this work, the SSR method is employed in connection with the ω PBEh range-separated hybrid density functional³⁰ and the 6-31G* basis set³¹. The geometries of the S_1 and S_0 state minima, S_1/S_0 conical intersections and the minimum energy paths (MEPs) were optimized using the SSR analytical energy derivatives formalism described in Ref.³². The SSR computations were carried out using the beta-testing version of the TeraChem® program (v1.92P, release 7f19a3bb8334)^{33–38}.

Building the S_1 and S_0 MEPs was carried out as follows: First, the geometries of the S_1 and S_0 minima were optimized for CHD and cZc-HT using the DL-FIND module³⁹ interfaced with TeraChem. Then, the S_1/S_0 conical intersection geometry was optimized using the CIOpt program⁴⁰ receiving the SSR energies and gradients from TeraChem output. Having obtained the S_1 and S_0 equilibrium geometries and the MECI geometry, the MEPs connecting these critical points were optimized using the nudged elastic band (NEB) method⁴¹ with fixed endpoints as implemented in DL-FIND. The MEPs comprise the following legs: (1) CHD- S_0 min – S_1/S_0 MECI, (2) CHD- S_1 FC – S_1/S_0 MECI, (3) S_1/S_0 MECI – cZc-HT- S_0 min and (4) S_1/S_0 MECI – cZc-HT- S_1 FC; the MEPs (1) and (3) are on the S_0 PES, the MEPs (2) and (4) are on the S_1 PES. The MEPs (1) and (2) comprise 20 NEB images, the MEPs (3) and (4) comprise 40 images each. At each point of the MEPs the relaxed density matrix for the respective state was calculated and analyzed with QTAIM and the stress tensor using the AIMAll⁴² suite on each wave-function obtained in the previous step.

4. Results and discussions

4.1. Analysis of the S_1 and S_0 states minimum energy pathways of the CHD ring-opening reaction

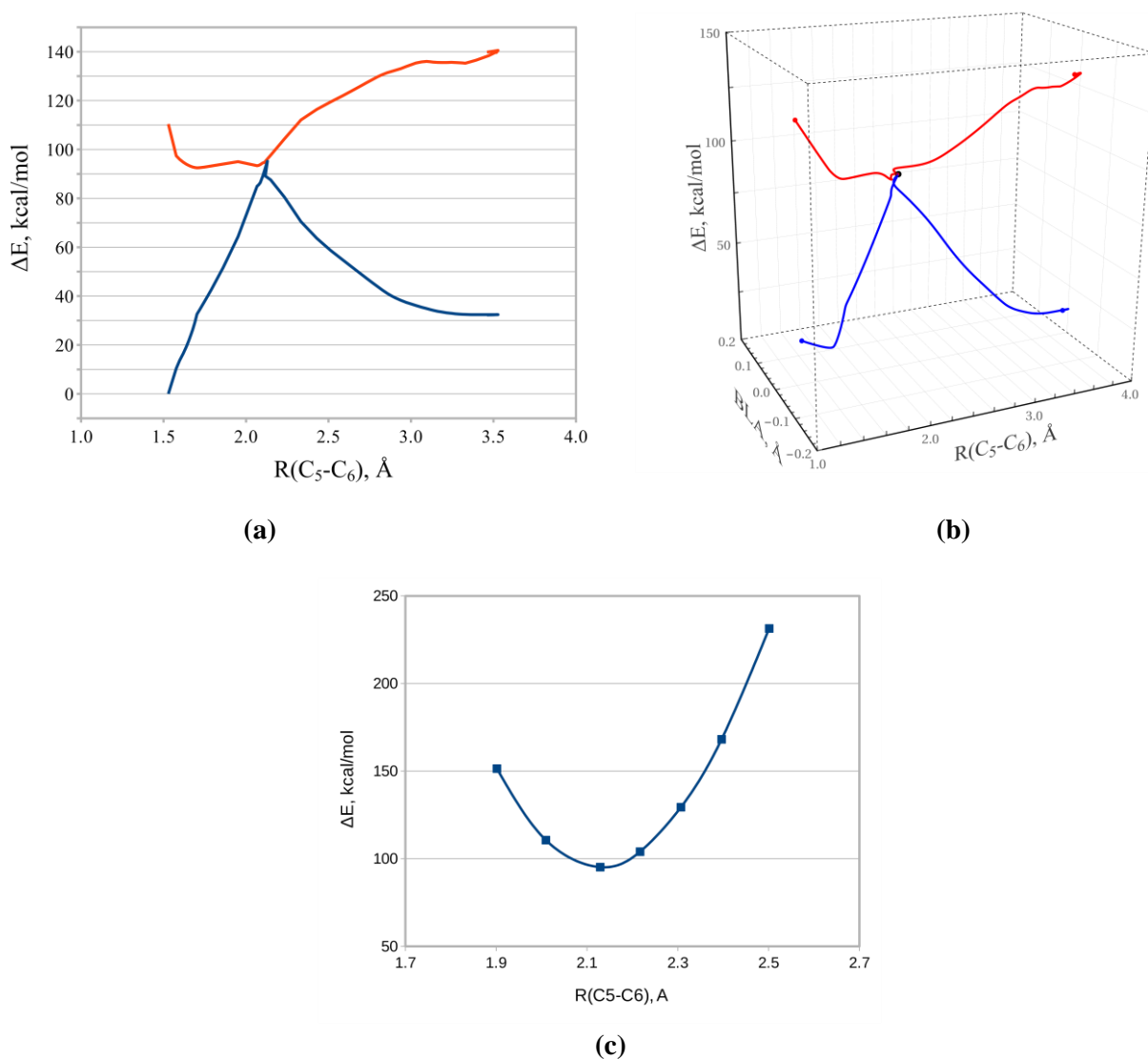


Figure 1. The variation of the 2-D and 3-D relative energy ΔE for the S_0 (blue) and S_1 (red) electronic states of the CHD \rightarrow HT photoreaction with $R(C_5-C_6)$ in Ångstrom are presented in the sub-figure (a-b) respectively. Additional relative energies ΔE of additional C.I. points along the S_1/S_0 C.I. seam of CHD are presented in sub-figure (c).

The geometries corresponding to the local minima on the S_1 and S_0 PESs of CHD and the S_1/S_0 MECI optimized in this work using the SSR- ω PBEh/6-31G* method are shown in **Scheme 1** and **Scheme 2**. The S_0 -min CHD geometry obtained is in a reasonable agreement with the experimental geometry available in the literature⁴³. The S_1/S_0 MECI geometry is in good agreement with the recent MSPT2 geometry from ref.¹².

Profiles of the S_0 and S_1 PESs along the MEPs of the ring-opening of CHD demonstrate that the photoexcitation at the S_0 equilibrium geometry of CHD is achieved by the $\pi \rightarrow \pi^*$ one-electron transition, which weakens the double bonds of the CHD ring, see **Figure 1**, **Scheme 1** and **Scheme 2**. Simultaneously with the π -bonds, the C5-C6 σ -bond is slightly weakened by the excitation. At the C_2 geometry, the σ -bonding orbital is mixed with the π -type HOMO and depletion of the electron density in the HOMO leads to weakening of the σ -bond. The excitation leads to stretching of the former π -bonds and the C5-C6 σ -bond

of CHD and the S_1 MEP slides down to the S_1 minimum, which occurs at a C_2 geometry with a stretched C5-C6 bond and π -bonds of CHD. The profile of the MEP where the S_1 and S_0 relative energies ΔE are shown as functions of the C5-C6 bond length and the bond-length-alternation (BLA) distortion is presented in the 3-D plot in **Figure 1(b)**. At the beginning of the S_1 MEP, the BLA coordinate undergoes a rapid change from a positive value (double bonds shorter than single bonds) to a near zero value (double and single bonds are nearly equal in length).

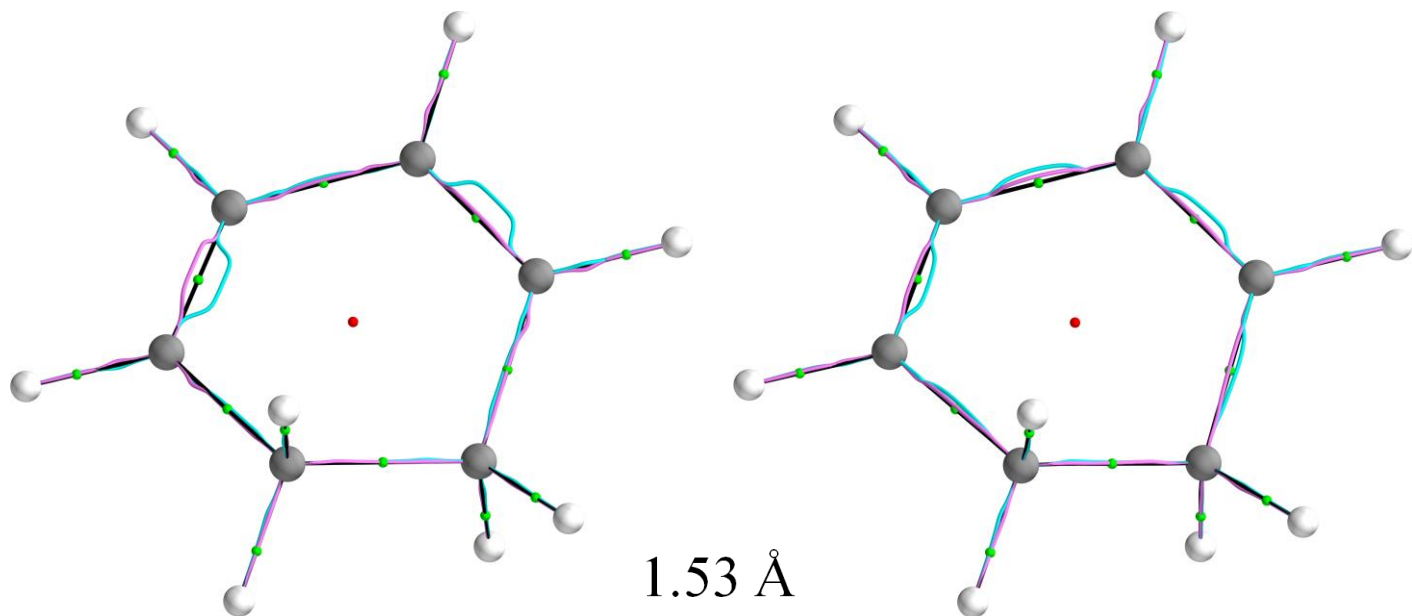
After the S_1 minimum, the MEP follows in the direction of the MECI point, which occurs at a geometry distorted away from the C_2 -symmetry. The MECI geometry corresponds to a six-membered ring, where the C5-C6 bond is stretched to 2.129 Å. This agrees well with the geometry obtained by the MSPT2 method. The earlier CASSCF calculations yielded a five-membered ring geometry corresponding to the MECI, with the C1-C5 bond (referred to as the C4---C6 *BCP* in this work, see **Scheme 2**) shorter than the C5-C6 bond. The CASSCF method, however, neglects the dynamic electron correlation. The inclusion of the dynamic correlation in the SSR (and in the MSPT2) method has considerable implications for the geometry of the S_1/S_0 MECI of CHD.

Having crossed the MECI point, the S_0 MEP continues to the *cZc*-HT S_0 minimum without any hindrance. Similarly, the S_0 MEP leading to the original CHD conformation is barrierless and steep. There is however, an indication that the MECI→HT stretch of the S_0 MEP first goes in the direction of shorter C5-C6 bond and then turns to stretching of the bond, see **Figure 1(a)**. This implies the existence of an attractive interaction between the C5 and C6 atoms in the vicinity of the MECI geometry.

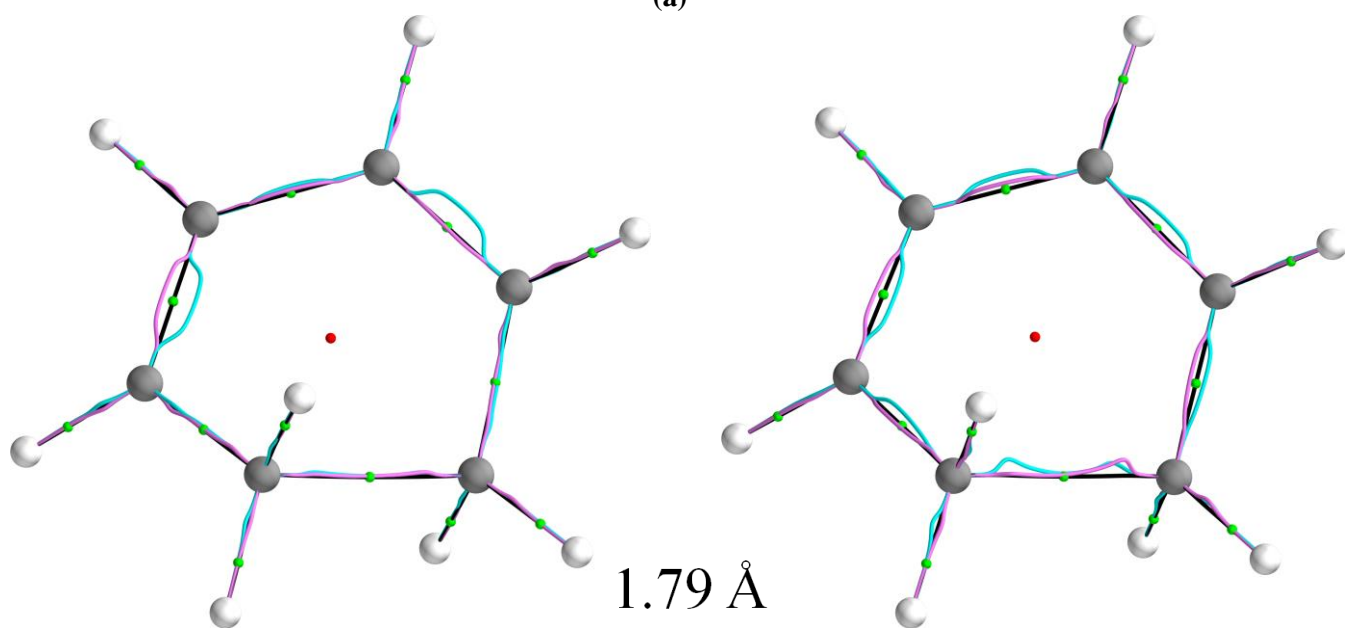
To investigate whether the attractive interaction is present at C.I. geometries with a stretched C5-C6 bond-length, a number of *additional* C.I.s along the S_1/S_0 seam were optimized with the bond-length varying in the range of 1.9 Å to 2.5 Å. The relative energies ΔE of the C.I.s (with respect to CHD S_0 -min) are presented in **Figure 1(c)**. The C.I. points studied here cover sufficiently large energy range; up to 150 kcal/mol above the MECI point. The presence of an attraction between C5 and C6 atoms for the higher energy C.I.s implies that the C5-C6 bond is central to controlling the dynamics of CHD ring-opening. Therefore, the presence of the C5-C6 bonding interaction for stretched bond-lengths should steer the reaction toward CHD and opening of the ring can occur if there is a sufficiently large and persistent momentum pointing in the direction of the stretching of the C5-C6 bond.

4.2. A QTAIM bond-path analysis of the CHD ring-opening reaction

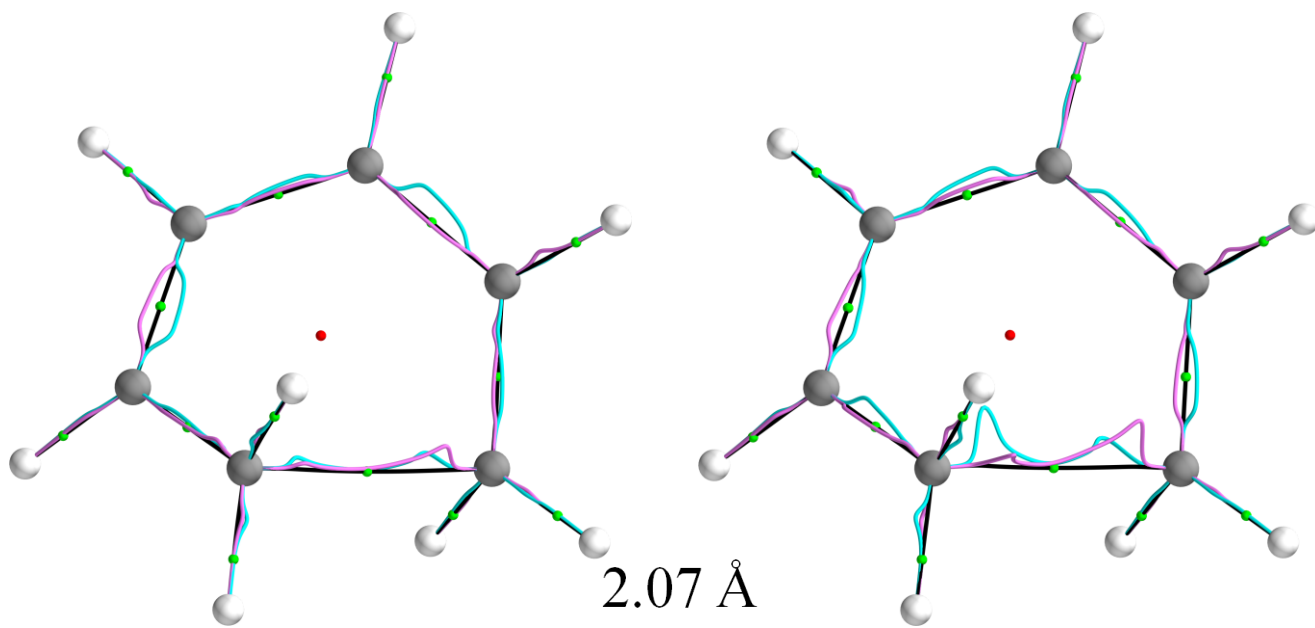
In this section we will refer to the MEPs outlined in section 4.1 in the context of the complete 3-D bond-path framework set $\mathbb{B} = \{(\mathbf{p}_0, \mathbf{p}_1), (\mathbf{q}_0, \mathbf{q}_1), \mathbf{r}\}$ and the bond-path ellipticity ε profiles to quantify the increase in closed-shell *BCP* character of the shared-shell C5-C6 *BCP* as the ring-open reaction proceeds, see **Figure 2** and **Figure 3** respectively.



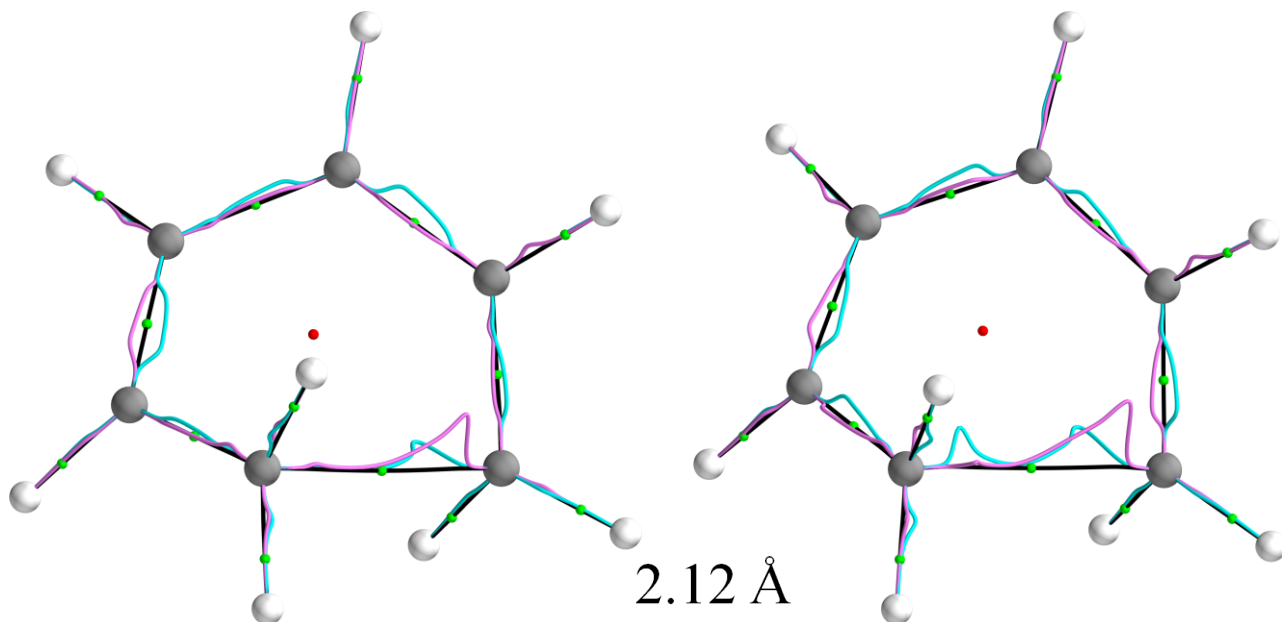
(a)



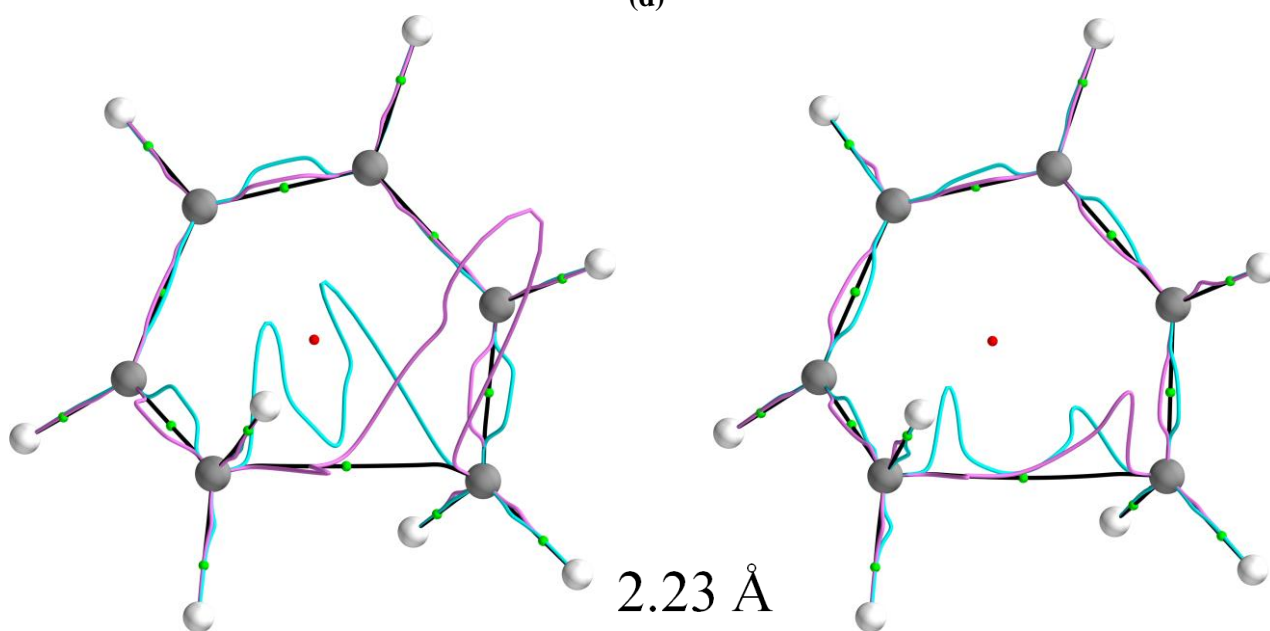
(b)



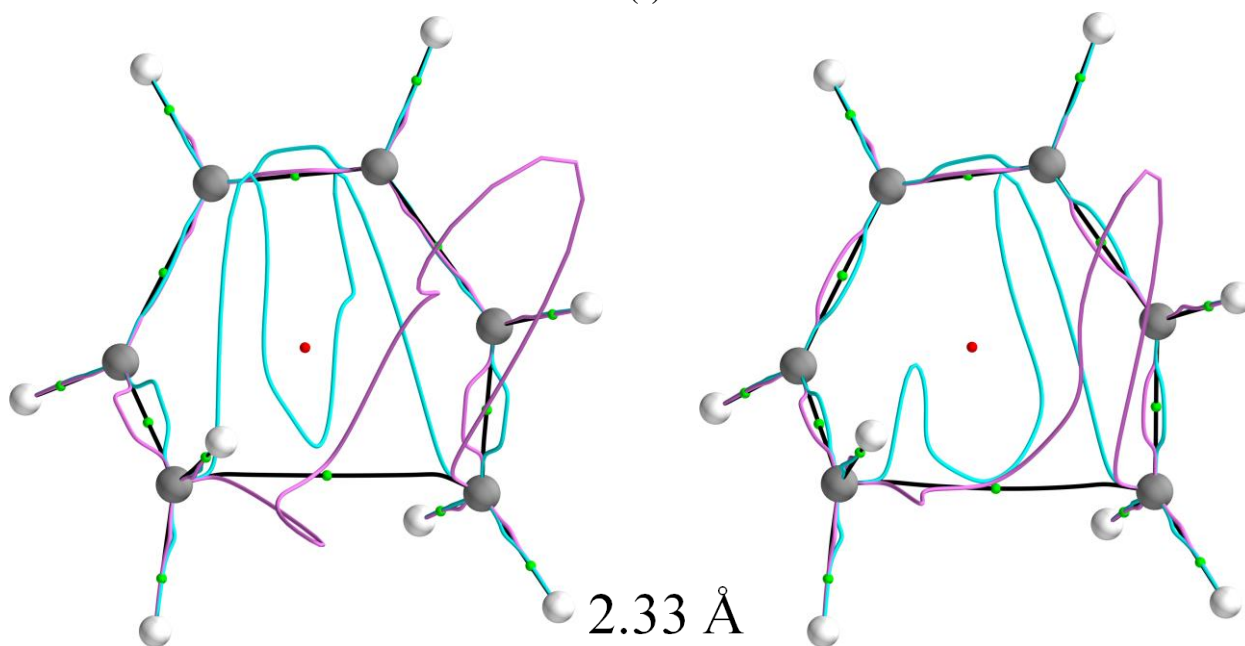
(c)



(d)



(e)



(f)

Figure 2. The p_0 - and q_0 -paths for the S_0 state (left panel) and corresponding p_1 - and q_1 -paths S_1 state (right panel) electronic states of the C5-C6 *BCP* bond-path for the CHD→HT photoreaction molecular graph subjected to the bond-length $R(\text{C5-C6})$ distortion for 1.53 Å, 1.79 Å, 2.07 Å, 2.12 Å, 2.23 Å and 2.33 Å are presented in sub-figures (a)-(f) respectively. The undecorated green and red spheres indicate the positions of the bond critical points (*BCPs*) and ring critical points (*RCP*), see also **Figure 1** and **Scheme 2** for the atom numbering scheme.

Examination of the p_0 - and q_0 -paths and p_1 - and q_1 -paths for the S_0 and S_1 states respectively indicates that the reaction at CHD commences with a mix of double and single bond character bonds. Double and single bond character is indicated by the presence of the (p_0, q_0) or (p_1, q_1) -paths that display larger or smaller deviations around the *BCP* associated with the bond-path; note, the (p_0, q_0) or (p_1, q_1) -paths may be obscured by being normal to the plane of the molecule, see **Figure 2**.

The weakening of the double bonds of the CHD ring due to the CHD→HT photoreaction is evident from the smaller deviations of the (p_1, q_1) -paths compared with the (p_0, q_0) -paths, hence lower ellipticity ε values, away from the C3-C4 *BCP* and C1-C2 *BCP* bond-paths (r), shown in the left and right panels of **Figure 2(a)**, also see **Scheme 2**. The photoexcitation leads to stretching of the bond-path (r) of the C5-C6 *BCP* and results in longer (p_1, q_1) -paths than (p_0, q_0) -paths as the S_1 MEP slides down to the S_1 minimum; simultaneously it leads to the creation of higher ellipticity ε (π -bonds) of CHD ring.

We notice that after the MECI point ($R(\text{C5-C6})= 2.12\text{\AA}$) the (p_0, q_0) and (p_1, q_1) -paths associated with the C5-C6/C5--C6 *BCP* drastically stretches signifying the transition in chemical character from the (C5-C6 σ -bond) shared-shell C5-C6 *BCP* to the closed-shell C5--C6 *BCP*. In addition, after the MECI point the q_0 - and q_1 -paths (indicate the most preferred direction of motion of $\rho(\mathbf{r}_b)$) are clearly directed normally to the plane of the CHD ring and not towards the *RCP* (undecorated red sphere at the centre of the CHD ring) that would be the case for an unstable closed-shell *BCP*. The eventual direction of rupture of the closed-shell C5--C6 *BCP* is indicated by the q_0 - and q_1 -paths.

Before the MECI point is reached, the ellipticity ε profiles indicate that the values of the ellipticity ε are higher for the S_1 than for the S_0 state, see **Figure 3(a-c)**; the converse being true after the MECI point, see **Figure 3(d-f)**. The ellipticity ε profiles demonstrate that throughout the duration of the CHD ring-opening there is an increasing tendency for the $\rho(\mathbf{r}_b)$ to accumulate towards the C5 *NCP* and C6 *NCP*. This demonstrates an increase in closed-shell *BCP* character and therefore dominance of the positive λ_3 eigenvalue resulting in a value of the Laplacian $\nabla^2\rho(\mathbf{r}_b) > 0$, where $\nabla^2\rho(\mathbf{r}_b) = \lambda_1 + \lambda_2 + \lambda_3$ and is entirely consistent with the behavior of closed-shell *BCPs*. Note that the Hessian eigenvalues are ordered as $\lambda_1 < \lambda_2 < \lambda_3$, and we always have $\lambda_1 < 0$ and $\lambda_2 < 0$. Therefore, the increase in the magnitude of the peaks in the (p_0, q_0) and (p_1, q_1) -paths towards C5 *NCP* and C6 *NCP* displays the variation in closed-shell *BCP* character along the bond-path of the C5-C6/C5--C6 *BCP*.

In the next section, we explore the mixture of shared-shell *BCP* character of the closed-shell C5--C6 *BCP*.

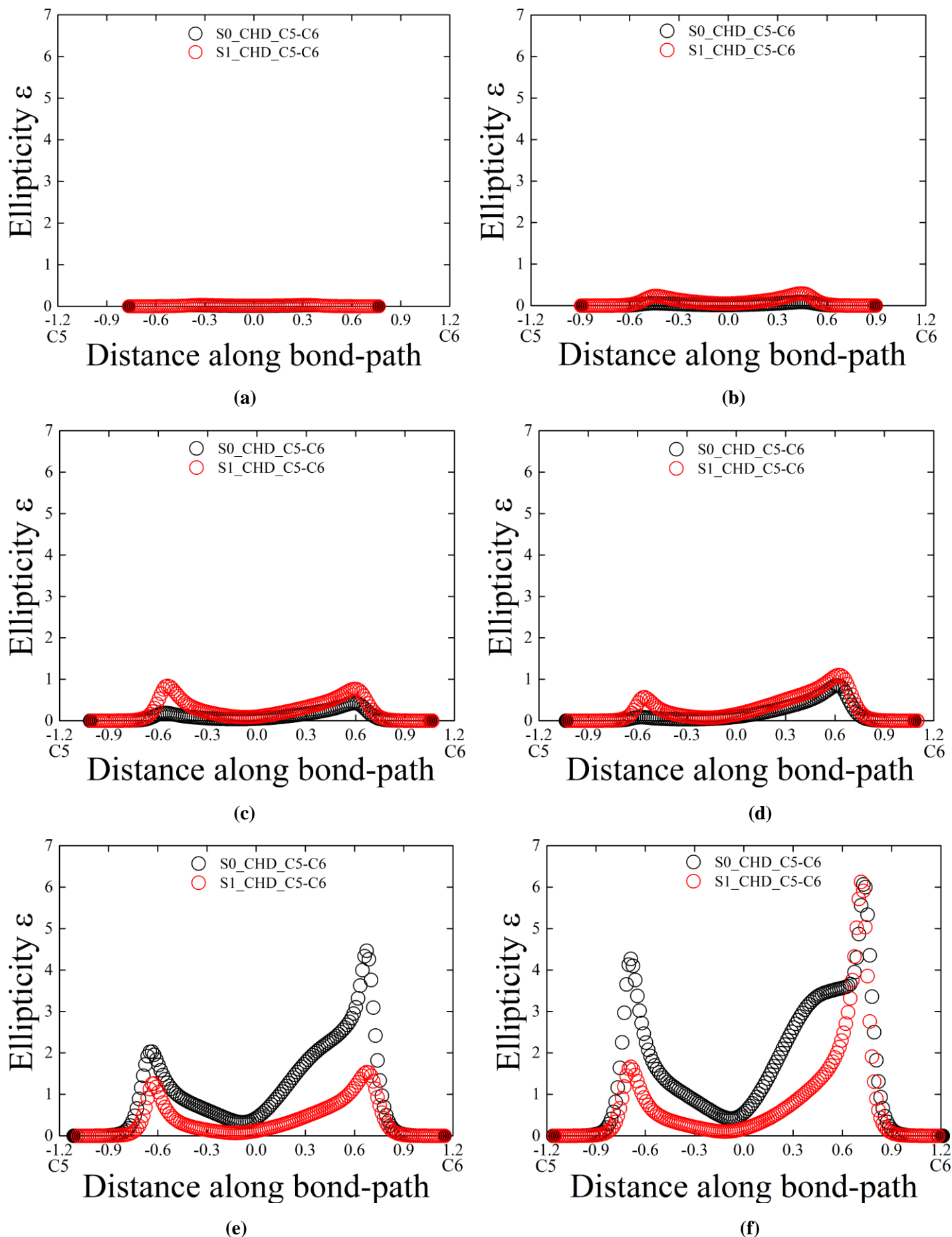
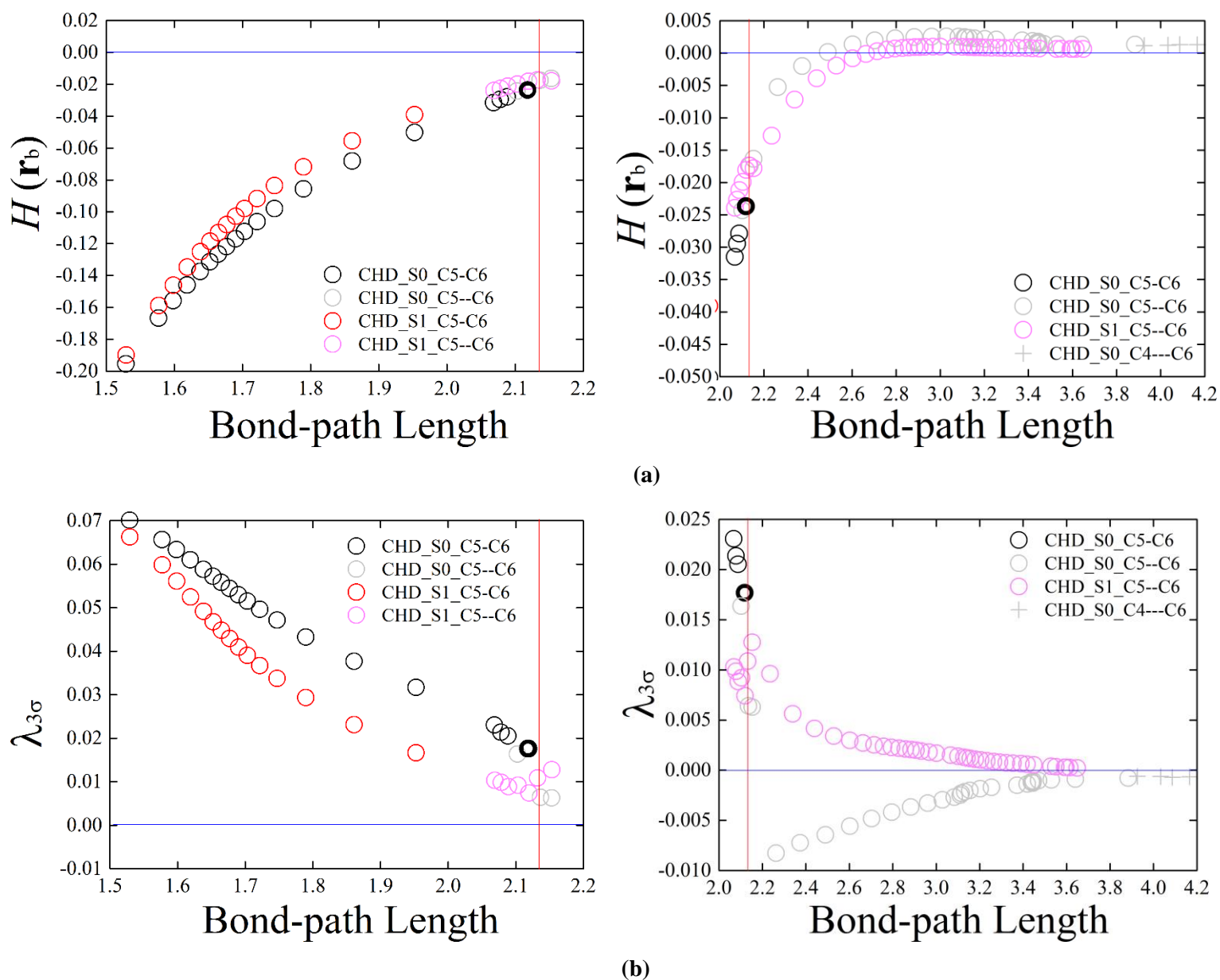


Figure 3. The ellipticity ε profiles along the bond-path of the C5-C6 *BCP* for the CHD \rightarrow HT photoreaction molecular graph corresponding to bond length $R(C5-C6)$ distortions of 1.53 Å, 1.79 Å, 2.07 Å, 2.12 Å, 2.23 Å and 2.33 Å in the S_0 and S_1 electronic states are presented in sub-figures (a)-(f), see **Scheme 2** for the atom labelling scheme.

4.3. A QTAIM and stress tensor BCP analysis of the CHD ring-opening reaction

In section 4.2 we tracked the increase in closed-shell *BCP* character of the shared-shell C5-C6 *BCP* from the start of the CHD→HT photoreaction. In this section we mainly focus on quantifying the mixture of shared-shell C5-C6 *BCP* (C5-C6 σ -bond) character of the closed-shell C5--C6 *BCP* as measured by the presence of values of the total local energy density $H(\mathbf{r}_b) < 0$. We also include the temporary C4---C6 *BCP*, see **Figure 4**, which is referred to as the C1-C5 bond in the grey scale sketches of the left panel of **Scheme 2**. We also consider the changes to the topological stability from values of the stress tensor eigenvalue $\lambda_{3\sigma} < 0$ and increase in the ellipticity ε that is known to indicate a decrease in stability for closed-shell *BCPs*, see **Figure 4(b)** and **Figure 4(c)**, respectively. To display the variations of the $H(\mathbf{r}_b)$, $\lambda_{3\sigma}$ and the ellipticity ε values with the bond-path length (BPL) over both the shared-shell *BCP* and closed-shell *BCP* regimes with clarity and continuity we split the results across overlapping ranges of bond-path length values, (BPL = 1.5 Å to 2.2 Å) and (BPL = 2.0 Å to 4.2 Å) in the left and right panels of **Figure 4(a-c)**.



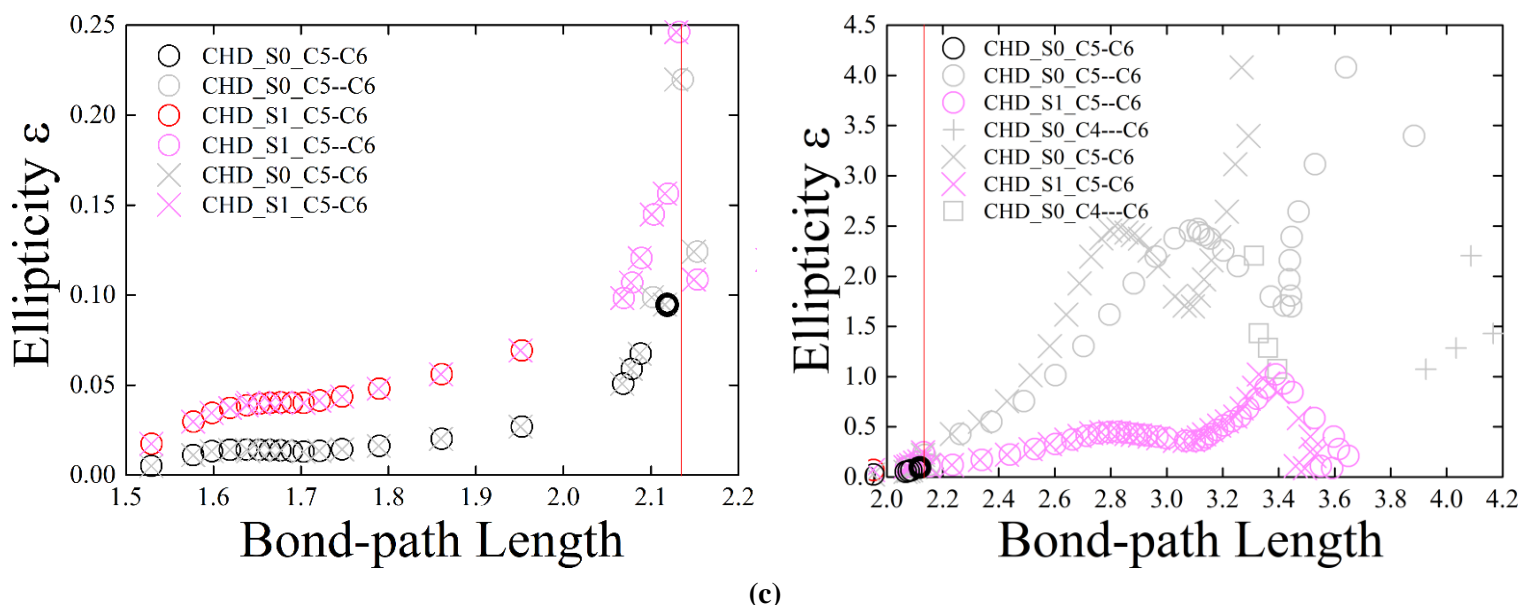


Figure 4. The variation of the local total energy density $H(\mathbf{r}_b)$, stress tensor eigenvalue $\lambda_{3\sigma}$ and ellipticity ε for S_0 (grey) and S_1 (pale-magenta) with the bond-path length (BPL) in Å of the closed-shell C5--C6 BCP (circle) and C4---C6 BCP (cross) for the of the CHD→HT photoreaction molecular graph are presented in sub-figures (a-c) respectively. The horizontal blue line and vertical red lines correspond to values of $H(\mathbf{r}_b) < 0$ and the position of the conical intersection (C.I.), respectively see **Scheme 2** and **Figure 1(a-b)**. Note, for the S_0 state the bold black circle corresponds to a point on the MEP beyond the C.I. Values of $H(\mathbf{r}_b) < 0$ and the MECI point are highlighted by the horizontal blue line and the vertical red line respectively. The shared-shell BCPs (denoted by "--") and closed-shell BCPs where $H(\mathbf{r}_b) < 0$ and $H(\mathbf{r}_b) > 0$ are denoted by "---" and "----" respectively in the legends.

At the start of the reaction the fissile C5-C6 bond is a shared-shell C5-C6 BCP, indicated by the black and red circles for the S_0 and S_1 states respectively, see **Scheme 1**, **Scheme 2** and the left panels of **Figure 4(a-c)**. Before the MECI the C5-C6 BCP is stronger in the S_0 than the S_1 state as indicated by more negative values $H(\mathbf{r}_b)$ and more topologically stable as determined by more positive values of $\lambda_{3\sigma}$ associated with the S_0 state. Also before the MECI, the ellipticity ε is lower in the S_0 than the S_1 state consistent with stronger shared-shell BCPs. In the S_0 state there is an oscillation in the chemical nature of the C5-C6 bond between the shared-shell C5-C6 BCP and closed-shell C5--C6 BCP, see the left panel of **Figure 4(a)**. The bold black circle (a shared-shell C5-C6 BCP) corresponds to a point on the S_0 MEP beyond the MECI but appears to occur before the MECI due to a contraction of the C5-C6 BCP bond-path resulting in transformation of the closed-shell C5--C6 BCP → shared-shell C5-C6 BCP. This oscillation provides evidence that the MECI→HT stretch of the S_0 MEP first goes in the direction of shortening the closed-shell C5--C6 BCP back to stronger shared-shell BCP before continuing with the stretching of the bond-path of the closed-shell C5--C6 BCP. We also notice that for S_0 the shared-shell C5-C6 BCP, indicated by the bold black circle, has a more positive value of $\lambda_{3\sigma}$ than the neighboring closed-shell BCP (grey circle) that possesses a shorter BPL, see **Figure 4(a)**. This indicates that the highlighted (bold black circle) shared-shell C5-C6 BCP is more topologically stable than the neighboring closed-shell C5--C6 BCP.

For a value of $R(\text{C5-C6}) = 2.12$ Å the S_0 state corresponds to the shared-shell C5--C6 BCP in contrast to the closed-shell C5--C6 BCP for the S_1 state, see the left and right panels of **Figure 2(d)** respectively, see also

the **Supplementary Materials S5**. This demonstrates that for the S_0 state there is an attractive interaction between the $C5$ *NCP* and $C6$ *NCP* in the vicinity of the MECI point and an attraction beyond the MECI geometry up to at least 2.5 Å, see **Figure 5**.

Differences in the variation with the ellipticity ε of the $C5$ *NCP* and $C6$ *NCP* separation (S_0 and S_1 indicated by pale-magenta and grey 'X' respectively), compared with the bond-path length demonstrate bond stretching before and after the MECI point, see the left and right panels of **Figure 4(c)** respectively. The stretching of the $C5$ - $C6$ *BCP* bond-path is particularly large for the S_0 state and much larger than for the S_1 state, after the MECI point, explaining why the MEP continues to the *cZc*-HT S_0 minimum without hindrance, see the right panel of **Figure 4(c)**.

In the S_0 state the shared-shell $C5$ - $C6$ *BCP* persists further along the MEP than in the S_1 state, see the right panels of **Figure 4(a-c)**. Along the MEP in the S_1 state values of the Laplacian $\nabla^2\rho(\mathbf{r}_b) < 0$ corresponding to the shared-shell $C5$ - $C6$ *BCP* transforms smoothly to values of $\nabla^2\rho(\mathbf{r}_b) > 0$, which correspond to the closed-shell $C5$ -- $C6$ *BCP*, indicated by the pale-magenta circles in **Figure 4(a-c)**.

The mixed chemical character of the $C5$ - $C6$ σ -bond discussed in section 4.1 was explained in terms of the σ -bonding orbital is mixing with the π -type HOMO and depletion of the electron density in the π -orbital resulting in the weakening and stretching of the $C5$ - $C6$ σ -bond. The stretching results in the transition from the shared-shell $C5$ - $C6$ *BCP* to the closed-shell $C5$ -- $C6$ *BCP* before the MECI point, see **Figure 4**.

We can quantify the mixed chemical character in terms of the existence of values of $H(\mathbf{r}_b) < 0$ for the closed-shell $C5$ -- $C6$ *BCP*, that indicates a degree of coupling between the $C5$ -- $C6$ *BCP* and neighboring shared-shell *BCPs*, see **Figure 4(a)**. As the ring-opening reaction proceeds, the closed-shell *BCPs* retain a degree of shared-shell *BCP* character, i.e. $H(\mathbf{r}_b) < 0$, beyond the MECI point with lower values for the S_0 than for the S_1 state, see the right panel of **Figure 4(a)**. This is consistent with the finding that after the MECI point, the MEP continues to the *cZc*-HT S_0 minimum without hindrance. In addition, after the MECI point the values for $\lambda_{3\sigma}$ in the S_0 state become less *negative* despite the stretching of the $C5$ -- $C6$ *BCP* bond-path, conversely the values for $\lambda_{3\sigma}$ in the S_1 state become less positive, see **Figure 4(b)**. For the S_0 state the $C4$ --- $C6$ *BCP* (referred to as the $C1$ - $C5$ bond in left panel of **Scheme 2**) temporarily exists and for all values the $C4$ --- $C6$ *BCP* is weak (since $H(\mathbf{r}_b) > 0$) and topologically unstable, $\lambda_{3\sigma} < 0$, see the right panels of **Figure 4(a)** and **Figure 4(b)** respectively.

A number of *additional* C.I.s along the S_1/S_0 seam were optimized with the bond-path $C5$ - $C6$ *BCP* in the range of 1.9 Å to 2.5 Å, see **Figure 5**. The C.I. points investigated cover sufficiently large energy range; up to 150 kcal/mol above the MECI point, see **Figure 1(c)**. The results presented for the additional points along the C.I. seam show that for bond-path lengths of 2.5 Å the closed-shell $C5$ -- $C6$ *BCP* possesses a degree of covalent character i.e. $H(\mathbf{r}_b) < 0$ and therefore is “sticky” and resistant to moving towards the HT product until $H(\mathbf{r}_b) > 0$.

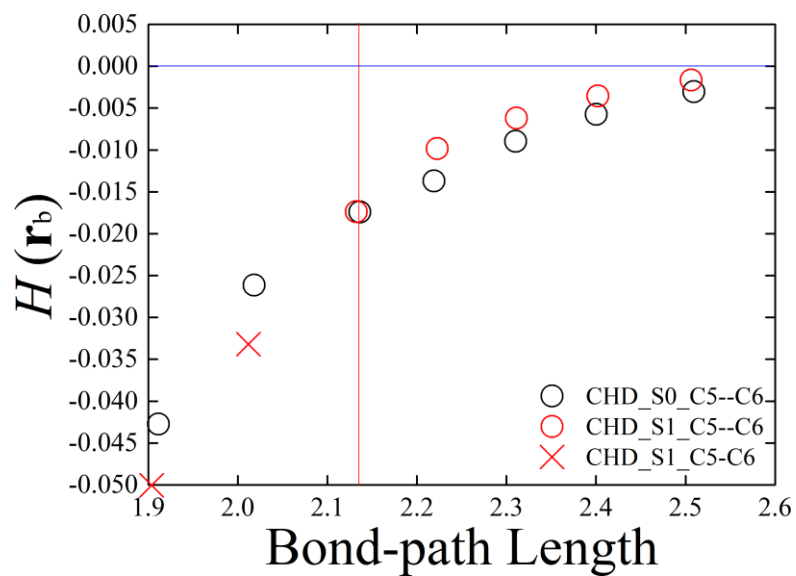


Figure 5. The variation of local total energy density $H(\mathbf{r}_b)$ for S_0 (black) and S_1 (red) with the bond-path length (Å) of the closed-shell C5--C6 *BCP* (circle) and shared-shell C5-C6 *BCP* (cross) for the of the CHD molecular graph are presented, see also **Figure 1(c)** and **Figure 4**.

Conclusions

We have investigated the CHD→HT photoreaction using the SSR method and analyzed the subsequent density matrices with our next generation QTAIM and stress tensor methodology to determine factors influencing the CHD→HT photoreaction branching ratio. Our calculations yielded a (60:40) CHD→HT photoreaction branching ratio that is closer to the experimental value of (70:30) than results obtained from the CASSCF method. The inclusion of the dynamic electron correlation in the SSR method yielded considerable differences in the geometry of the S_1/S_0 MECI of CHD compared with the previously and widely used CASSCF method that does not include dynamic electron correlation. For instance, earlier CASSCF calculations yielded a five-membered ring geometry corresponding to the MECI, with the C1-C5 bond (in this work we refer to as the C4---C6 *BCP*) shorter than the C5-C6 bond. In this investigation we find that the bond-path of the C1-C5 bond i.e. the C4---C6 *BCP*, is only present in the S_0 state and is longer than that of the fissile C5-C6 *BCP*/C5--C6 *BCP* contrary to previous CASSCF based calculations.

Further to this, we find using the QTAIM and stress tensor analysis that the C4---C6 *BCP* provides no measurable contribution to the geometry of the S_1/S_0 MECI of CHD because it is very weak and topologically unstable interaction and only present with very long bond-paths $> 3.8 \text{ \AA}$. The presence of an attraction between C5 and C6 atoms even at geometries corresponding to higher relative energies ΔE implies that the C5-C6 bond is central to controlling the dynamics of CHD ring-opening. Sufficient attraction exists between the C5 and C6 atoms in the S_0 electronic state on the CHD side of MECI point to cause the contraction of the closed-shell C5--C6 *BCP* bond-path to temporarily revert to the shared-shell C5-C6 *BCP*. From the QTAIM *BCP* analysis the closed-shell C5--C6 *BCP* is determined to be “sticky” on the basis of values of $H(\mathbf{r}_b) < 0$ that indicate a degree of covalent character and therefore coupling to the neighboring covalent (σ -bonds) C-H *BCPs*. This indicates that the reaction can be characterized as being pulled back towards CHD. Hence, this explains the origin of the (70:30) CHD ratio as being due to a “sticky” C5--C6 *BCP*.

We also investigate the CHD→HT photoreaction using the QTAIM bond-path analysis: the bond-path framework set $\mathbb{B} = \{(\mathbf{p}_0, \mathbf{p}_1), (\mathbf{q}_0, \mathbf{q}_1), \mathbf{r}\}$ and the bond-path ellipticity ε profiles. From this we demonstrate that the strong shared-shell C5-C6 *BCP* acquires closed-shell *BCP* character early on in the reaction process and this process starts closer CHD for the S_1 state than for the S_0 state.

Acknowledgements

The National Natural Science Foundation of China is gratefully acknowledged, project approval number: 21673071. The One Hundred Talents Foundation of Hunan Province and the aid program for the Science and Technology Innovative Research Team in Higher Educational Institutions of Hunan Province are also gratefully acknowledged for the support of S.J. and S.R.K.

References

1. W. Fuß, W. E. Schmid & S. A. Trushin. Time-resolved dissociative intense-laser field ionization for probing dynamics: Femtosecond photochemical ring opening of 1,3-cyclohexadiene. *Journal of Chemical Physics* **112**, 8347–8362 (2000).
2. Hofmann, A. & Vivieriedle, R. D. Quantum dynamics of photoexcited cyclohexadiene introducing reactive coordinates. *Journal of Chemical Physics* **112**, 5054–5059 (2000).
3. Marco Garavelli, †, Paolo Celani, ‡, Monica Fato, †, Michael J Bearpark, ‡, Barry R. Smith, ‡, Massimo Olivucci, †, And Robb, M.A., ‡. Relaxation Paths from a Conical Intersection: The Mechanism of Product Formation in the Cyclohexadiene/Hexatriene Photochemical Interconversion. *Journal of Physical Chemistry A* **101**, 2023–2032 (1997).
4. Celani, P., Ottani, S., Olivucci, M., Bernardi, F. & Robb, M. A. What Happens during the Picosecond Lifetime of 2A1 Cyclohexa-1,3-diene? A CAS-SCF Study of the Cyclohexadiene/Hexatriene Photochemical Interconversion. *Journal of the American Chemical Society* **116**, 10141–10151 (1994).
5. Paolo Celani, †, Fernando Bernardi, ‡, And, M. A. R., † & Massimo Olivucci, ‡. Do Photochemical Ring-Openings Occur in the Spectroscopic State? 1B2 Pathways for the Cyclohexadiene/Hexatriene Photochemical Interconversion. *Journal of Physical Chemistry* **100**, 19364–19366 (1996).
6. Adachi, S., Sato, M. & Suzuki, T. Direct Observation of Ground-State Product Formation in a 1,3-Cyclohexadiene Ring-Opening Reaction. *Physics Education* **35**, 202 (2015).
7. Tamura, H., Nanbu, S., Nakamura, H. & Ishida, T. A theoretical study of cyclohexadiene/hexatriene photochemical interconversion: multireference configuration interaction potential energy surfaces and transition probabilities for the radiationless decays. *Chemical Physics Letters* **401**, 487–491 (2005).
8. Hofmann, A. & Vivie-Riedle, R. D. Adiabatic approach for ultrafast quantum dynamics mediated by simultaneously active conical intersections. *Chemical Physics Letters* **346**, 299–304 (2001).
9. Tamura, H., Nanbu, S., Ishida, T. & Nakamura, H. Ab initio nonadiabatic quantum dynamics of cyclohexadiene/hexatriene ultrafast photoisomerization. *Journal of Chemical Physics* **124**, 1685–373 (2006).
10. Ohta, A., Kobayashi, O., Danielache, S. O. & Nanbu, S. Nonadiabatic ab initio Molecular Dynamics of Photoisomerization Reaction between 1,3-Cyclohexadiene and 1,3,5-cis-Hexatriene. *Chemical Physics* **459**, 45–53 (2015).
11. Pullen, S. H., Anderson, N. A., Ii, L. A. W. & Sension, R. J. The ultrafast photochemical ring-opening reaction of 1,3-cyclohexadiene in cyclohexane. *Journal of Chemical Physics* **108**, 556–563 (1998).
12. Mori, T. & Kato, S. Dynamic electron correlation effect on conical intersections in photochemical ring-opening reaction of cyclohexadiene: MS-CASPT2 study. *Chemical Physics Letters* **476**, 97–100 (2009).
13. Huang, W. J., Momen, R., Azizi, A., Xu, T., Kirk, S.R., Filatov, M. & Jenkins, S. A Vector-Based Representation of the Chemical Bond for the Ground and Excited States of Fulvene. (2018).
14. Bader, R. F. W. *Atoms in Molecules: A Quantum Theory*. (Oxford University Press, USA, 1994).
15. Bader, R. F. W. A Bond Path: A Universal Indicator of Bonded Interactions. *J. Phys. Chem. A* **102**, 7314–7323 (1998).
16. Bader, R. F. W. Bond Paths Are Not Chemical Bonds. *J. Phys. Chem. A* **113**, 10391–10396 (2009).
17. Ayers, P. W. & Jenkins, S. An electron-preceding perspective on the deformation of materials. *The Journal of Chemical Physics* **130**, 154104 (2009).
18. Jenkins, S., Kirk, S. R., Cote, A. S., Ross, D. K. & Morrison, I. Dependence of the normal modes on the electronic

structure of various phases of ice as calculated by ab initio methods. *Canadian Journal of Physics* **81**, 225-231(7) (2003).

19. Bone, R. G. A. & Bader, R. F. W. Identifying and Analyzing Intermolecular Bonding Interactions in van der Waals Molecules†. *J. Phys. Chem.* **100**, 10892–10911 (1996).

20. Maza, J. R., Jenkins, S. & Kirk, S. R. 11-cis Retinal Torsion: A QTAIM and Stress Tensor Analysis of the S1 Excited State. *Chemical Physics Letters* **652**, 112–116 (2016).

21. Jenkins, S., Maza, J. R., Xu, T., Jiajun, D. & Kirk, S. R. Biphenyl: A stress tensor and vector-based perspective explored within the quantum theory of atoms in molecules. *Int. J. Quantum Chem.* **115**, 1678–1690 (2015).

22. Wang, L., Guo, H., Momen, R., Azizi, A., Xu, T., Kirk, S.R., Filatov, M. & Jenkins, S. QTAIM and Stress Tensor Characterization of Intramolecular Interactions Along Dynamics Trajectories of a Light-Driven Rotary Molecular Motor. *J. Phys. Chem. A* **121**, 4778–4792 (2017).

23. Kraka, E. & Cremer, D. Description of chemical reactions in terms of the properties of the electron density. *Journal of Molecular Structure: THEOCHEM* **255**, 189–206 (1992).

24. Jenkins, S., Blancafort, L., Kirk, S. R. & Bearpark, M. J. The response of the electronic structure to electronic excitation and double bond torsion in fulvene: a combined QTAIM, stress tensor and MO perspective. *Phys. Chem. Chem. Phys.* **16**, 7115–7126 (2014).

25. Jenkins, S. & Heggie, M. I. Quantitative analysis of bonding in 90° partial dislocation in diamond. *Journal of Physics: Condensed Matter* **12**, 10325–10333 (2000).

26. Jenkins, S. & Morrison, I. The chemical character of the intermolecular bonds of seven phases of ice as revealed by ab initio calculation of electron densities. *Chemical Physics Letters* **317**, 97–102 (2000).

27. Ferré, N., Filatov, M. & Huix-Rotllant, M. Density-Functional Methods for Excited States. *Topics in Current Chemistry* **368**, VII–IX (2016).

28. Filatov, M. Assessment of Density Functional Methods for Obtaining Geometries at Conical Intersections in Organic Molecules. *Journal of Chemical Theory & Computation* **9**, 4526–4541 (2013).

29. Nikiforov, A., Gamez, J. A., Thiel, W., Huixrotllant, M. & Filatov, M. Assessment of approximate computational methods for conical intersections and branching plane vectors in organic molecules. *Journal of Chemical Physics* **141**, 124122 (2014).

30. Rohrdanz, M. A., Martins, K. M. & Herbert, J. M. A long-range-corrected density functional that performs well for both ground-state properties and time-dependent density functional theory excitation energies, including charge-transfer excited states. *Journal of Chemical Physics* **130**, 054112 (2009).

31. Dunning, T. H. Gaussian Basis Functions for Use in Correlated Molecular Calculations. I. The atoms B through Ne and H. (1989).

32. Filatov, M., Liu, F. & Martínez, T. J. Analytical derivatives of the individual state energies in ensemble density functional theory method. I. General formalism. *Journal of Chemical Physics* **147**, 197–163 (2017).

33. Ufimtsev, I. S. & Martínez, T. J. Quantum Chemistry on Graphical Processing Units. 1. Strategies for Two-Electron Integral Evaluation. *Journal of Chemical Theory & Computation* **4**, 222 (2008).

34. Ufimtsev, I. S. & Martinez, T. J. Quantum Chemistry on Graphical Processing Units. 2. Direct Self-Consistent-Field Implementation. *Journal of Chemical Theory & Computation* **5**, 1004 (2009).

35. Ufimtsev, I. S. & Martinez, T. J. Quantum Chemistry on Graphical Processing Units. 3. Analytical Energy Gradients, Geometry Optimization, and First Principles Molecular Dynamics. *Journal of Chemical Theory & Computation* **5**, 2619–2628 (2009).

36. Ufimtsev, I. S., Mart & Nez, T. J. Graphical Processing Units for Quantum Chemistry. *Computing in Science & Engineering* **10**, 26–34 (2008).

37. Titov, A. V., Ufimtsev, I. S., Luehr, N. & Martinez, T. J. Generating Efficient Quantum Chemistry Codes for Novel Architectures. *Journal of Chemical Theory & Computation* **9**, 213 (2013).

38. Song, C., Wang, L. P. & Martínez, T. J. Automated Code Engine for Graphical Processing Units: Application to the Effective Core Potential Integrals and Gradients. *Journal of Chemical Theory & Computation* **12**, 92 (2015).

39. Kästner, J., Carr, J.M., Keal, T.W., Thiel, W., Wander, A. & Sherwood, P. DL-FIND: an open-source geometry optimizer for atomistic simulations. *Journal of Physical Chemistry A* **113**, 11856 (2009).

40. Levine, B. G., And, J. D. C. & Martínez, T. J. Optimizing Conical Intersections without Derivative Coupling Vectors: Application to Multistate Multireference Second-Order Perturbation Theory (MS-CASPT2)†. *Journal of Physical Chemistry B* **112**, 405–13 (2008).
41. Jónsson., H., Mills, G. & Jacobsen, K. . In Classical and Quantum Dynamics in Condensed Phase Simulations. in *World Scientific Chapter 16*, 385–404 (1998).
42. Keith, T. A. *AIMAll, Revision 17.01.25*. (TK Gristmill Software, 2017).
43. K.H. Hellwege & A.M.Hellwege. *Landolt-Bornstein: Group II: Atomic and Molecular Physics. Structure Data of Free Polyatomic Molecules. 7*, (Springer, 1976).

SUPPLEMENTARY MATERIALS

Next-Generation Quantum Theory of Atoms in Molecules for the Ground and Excited State of the Ring-Opening of Cyclohexadiene (CHD)

Xin Bin¹, Tianlv Xu¹, Steven R. Kirk^{1*}, Michael Filatov^{1,2} and Samantha Jenkins^{1*}

Key Laboratory of Chemical Biology and Traditional Chinese Medicine Research and Key Laboratory of Resource Fine-Processing and Advanced Materials of Hunan Province of MOE, College of Chemistry and Chemical Engineering, Hunan Normal University, Changsha, Hunan 410081, China

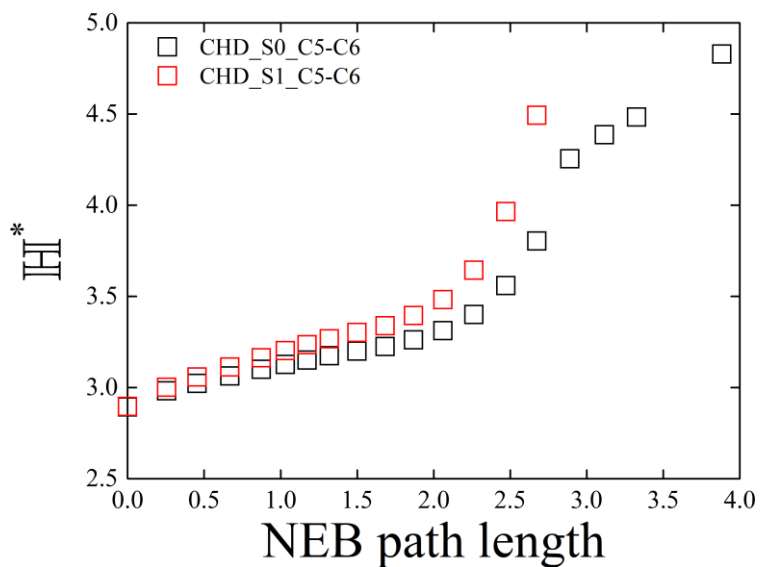
email: steven.kirk@cantab.net

email: mike.filatov@gmail.com

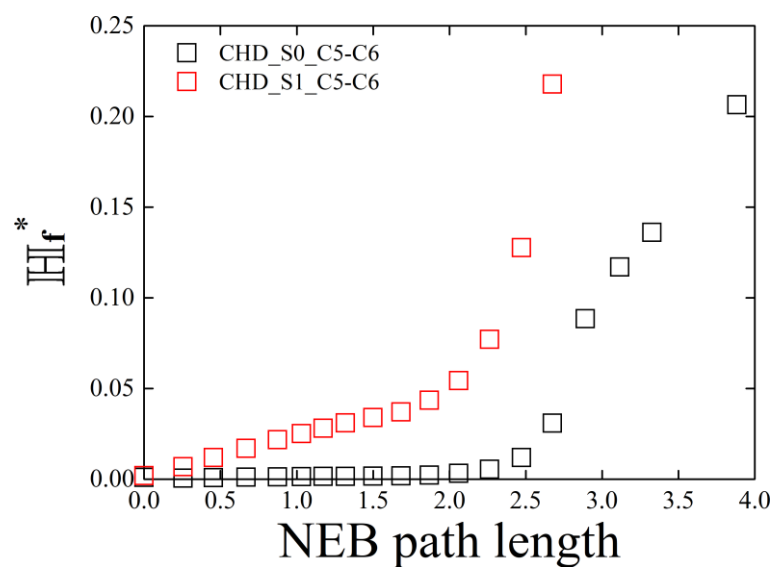
email: samanthajsuman@gmail.com

- 1. Supplementary Materials S1.** The variation of the eigenvector-following path length \mathbb{H}^* of the shared-shell C5-C6 *BCP* with the NEB path length.
- 2. Supplementary Materials S2.** The variation of \mathbb{H} of the closed-shell C5-C6 *BCP* with the NEB path length.
- 3. Supplementary Materials S3.** The variation \mathbb{H} of the C5-C6 *BCP* with the NEB path length.
- 4. Supplementary Materials S4.** Outline of the procedure to calculate \mathbb{B} , and discussion of the construction.
- 5. Supplementary Materials S5.** The p_0 - and q_0 -paths for the S_0 state in the vicinity of the C.I.

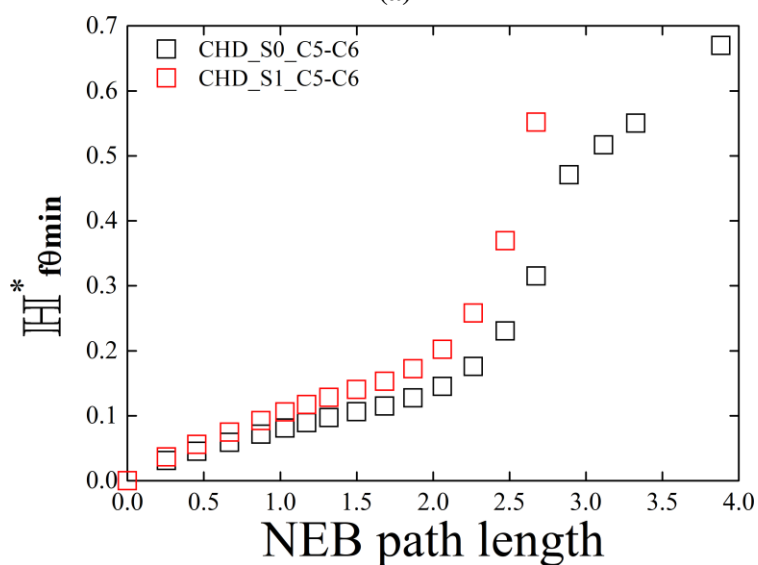
1. Supplementary Materials S1.



(a)



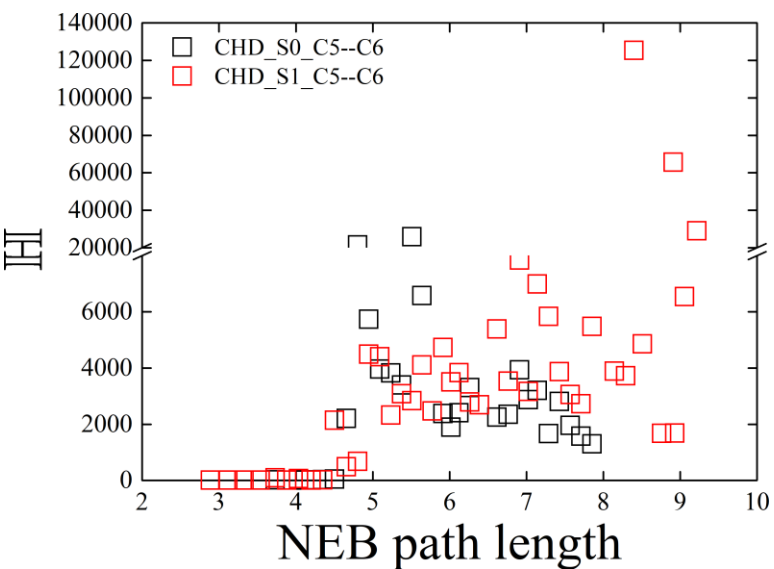
(b)



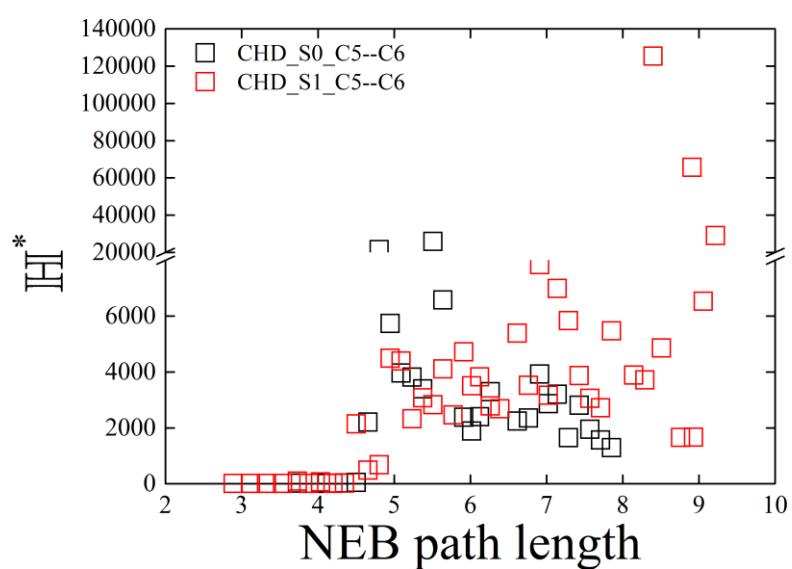
(c)

Figure S1. The variations of eigenvector-following path length H^* of the shared-shell (C5-C6 BCP) BCP are shown in (a). The variation of the fractional eigenvector-following path length H_f^* of the C5-C6 BCP are shown in (b). The variation of the $H_{f0min}^* = (H^* - H_{0min}^*)/H_{0min}^*$ of the C5-C6 BCP are shown in (c).

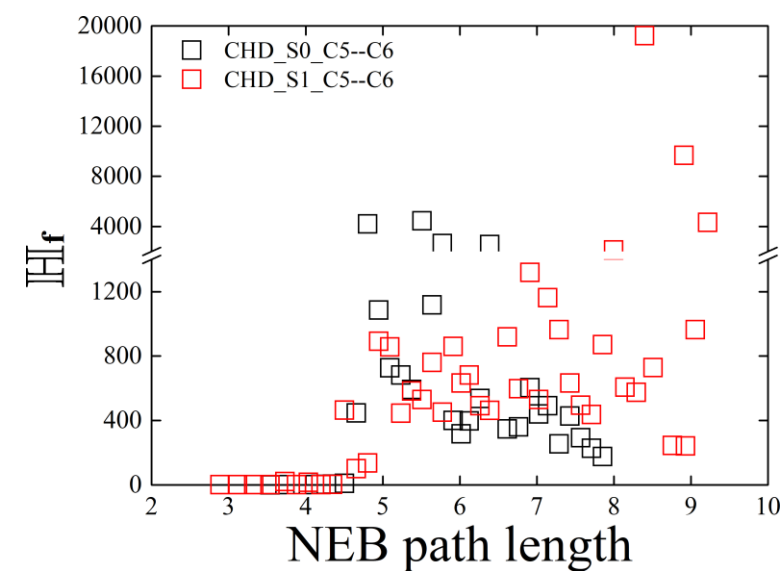
2. Supplementary Materials S2.



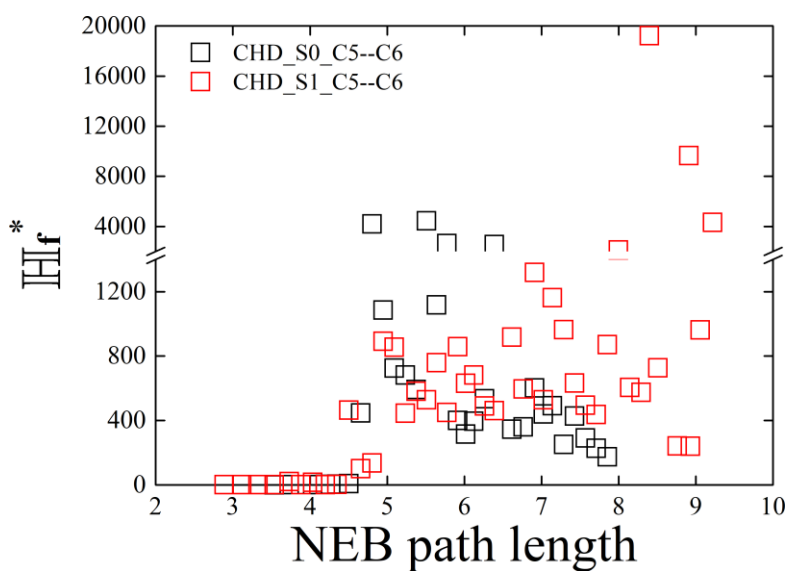
(a)



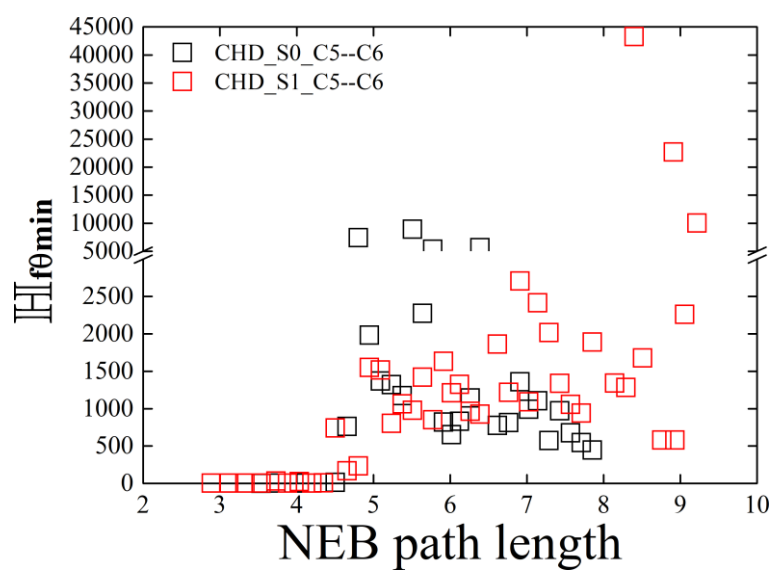
(b)



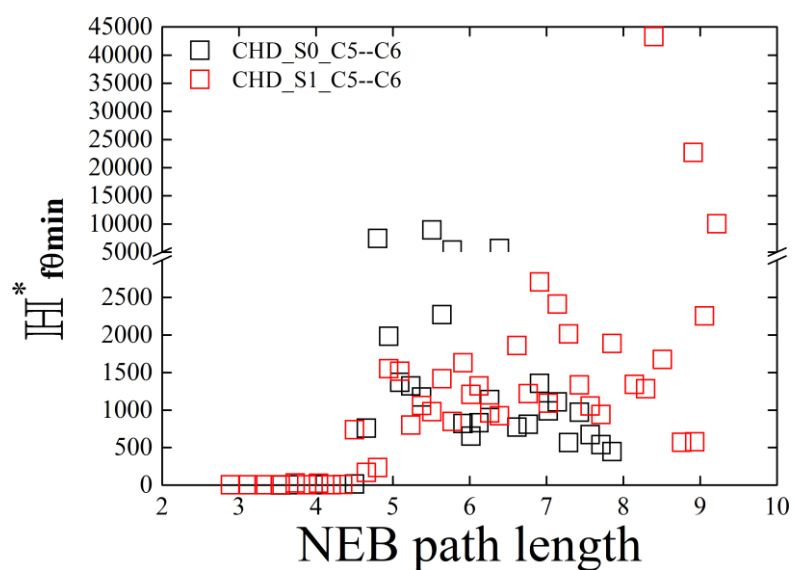
(c)



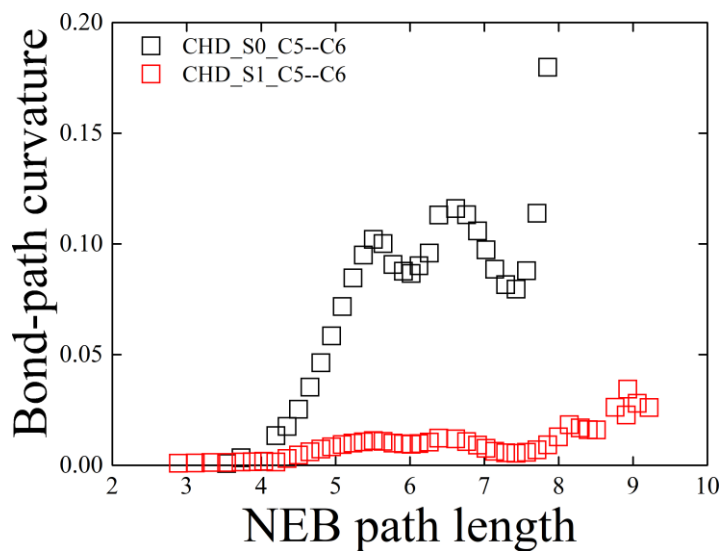
(d)



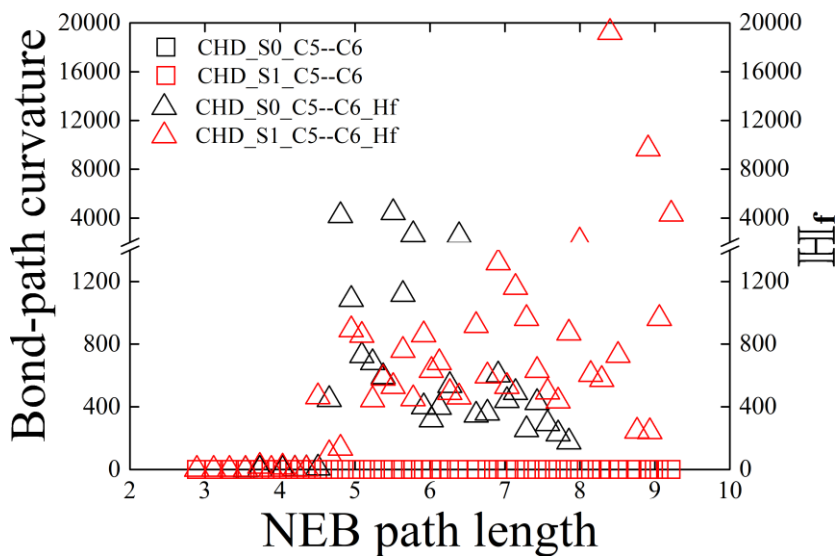
(e)



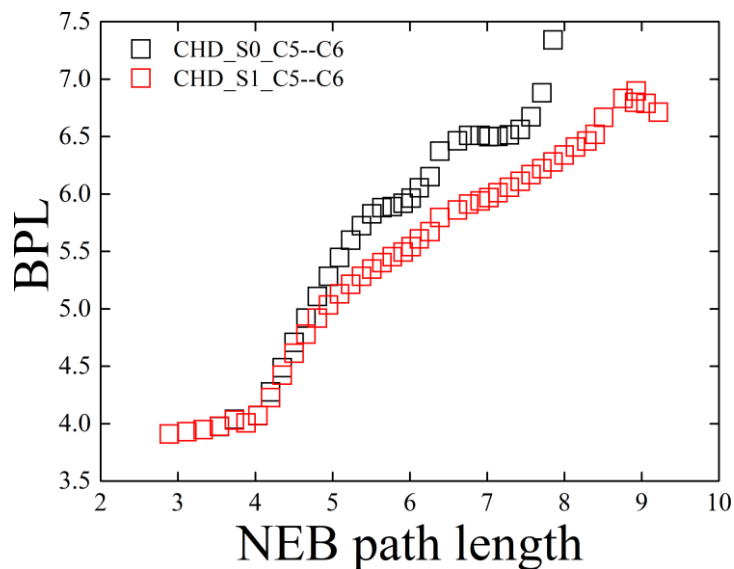
(f)



(g)



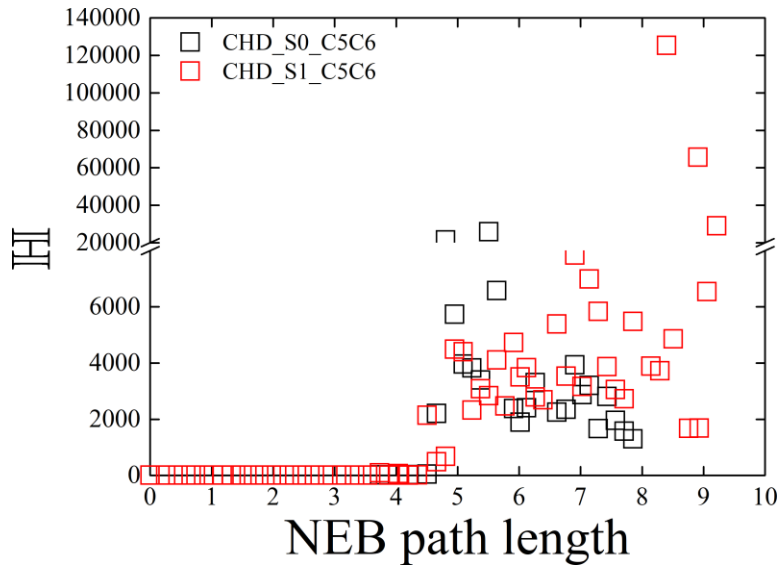
(h)



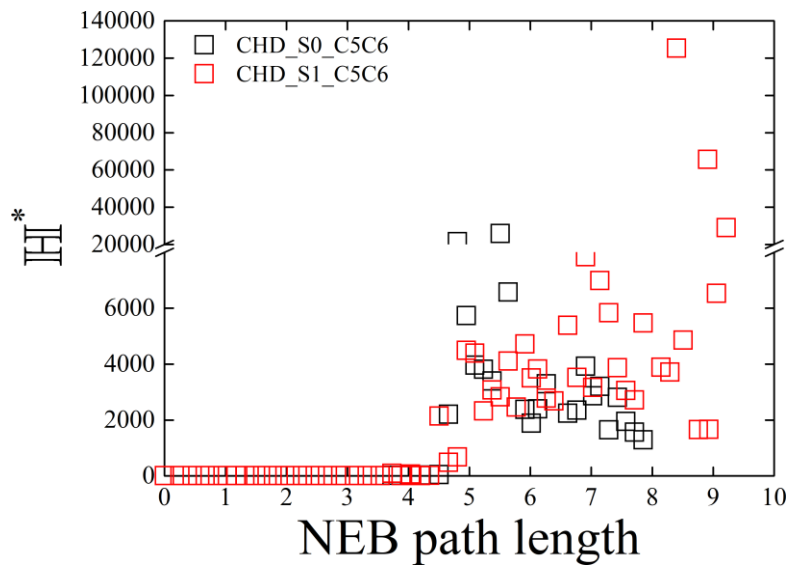
(i)

Figure S2. The eigenvector-following path length H and the corresponding variations eigenvector-following path length H^* of the closed-shell (C5-C6 BCP) BCP are shown in (a-b) respectively. The eigenvector-following path length H_f and the corresponding variation the fractional eigenvector-following path length H_f^* of the C5--C6 BCP are shown in (c-d) respectively. The variation of the $H_{f\theta\min} = (H_f - H_{f\theta\min})/H_{f\theta\min}$ and the corresponding value for $H_{f\theta\min}^* = (H_f^* - H_{f\theta\min}^*)/H_{f\theta\min}^*$ of the C5--C6 BCP are shown in (e-f) respectively. The variation of the bond-path curvature (BPL-GBL)/GBL and corresponding with H_f of the C5--C6 BCP are shown in (g-h). The variation of the bond-path lengths (BPL) of the C5--C6 BCP is shown in (i).

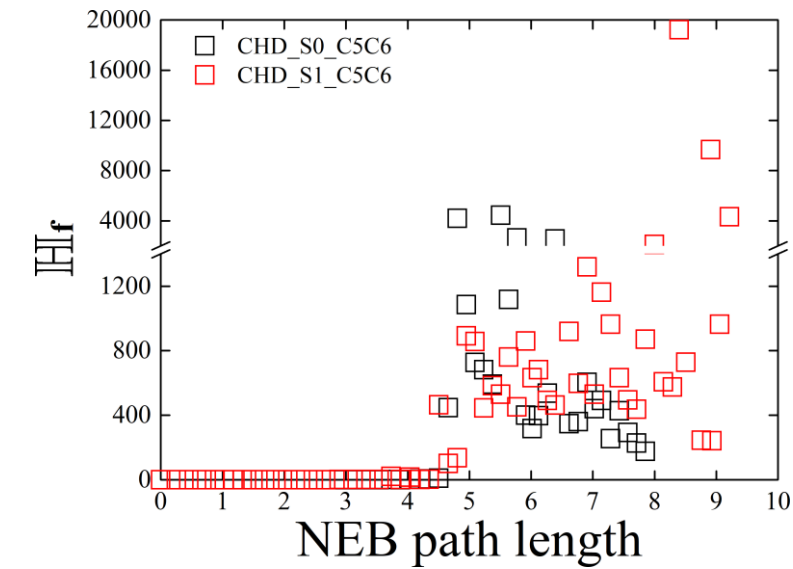
3. Supplementary Materials S3.



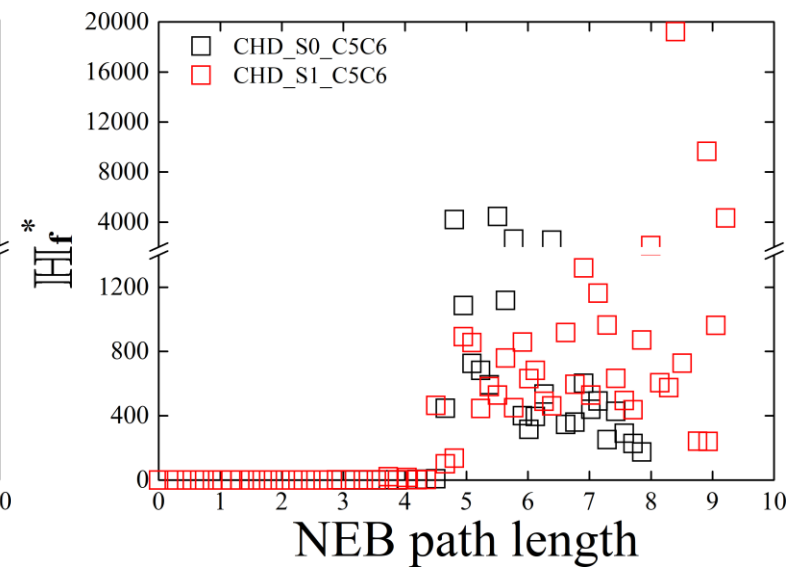
(a)



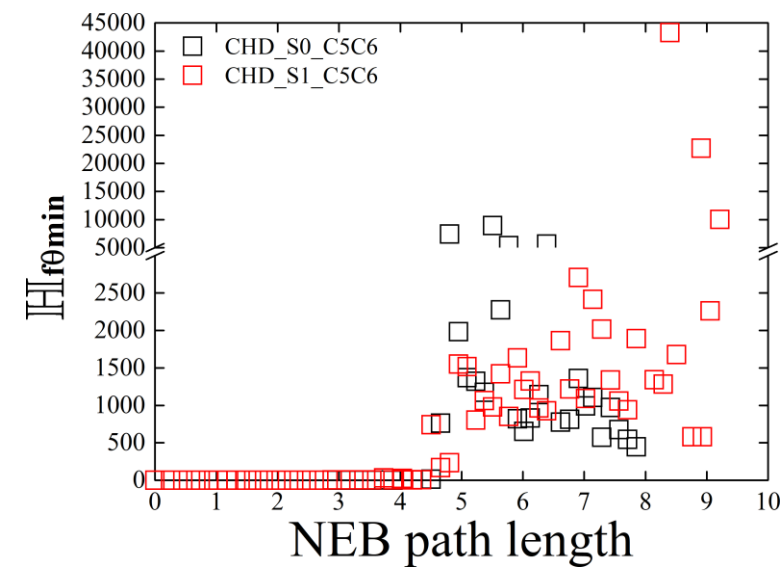
(b)



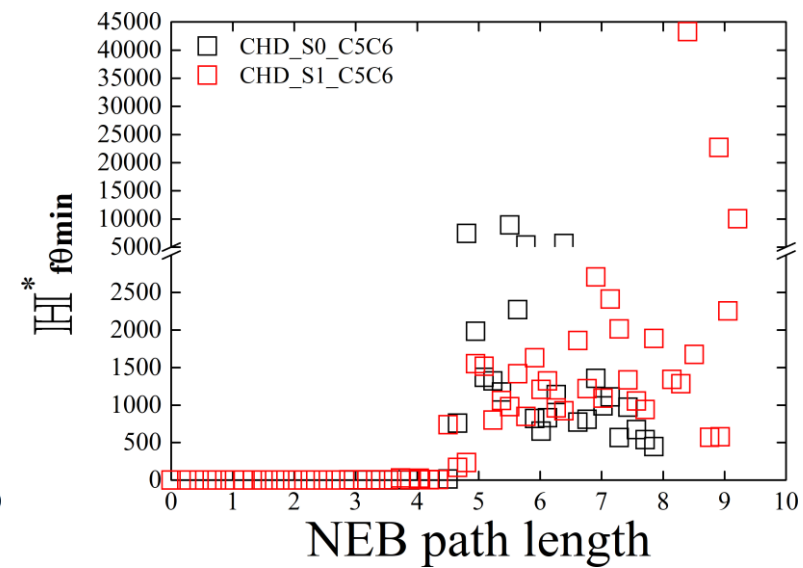
(c)



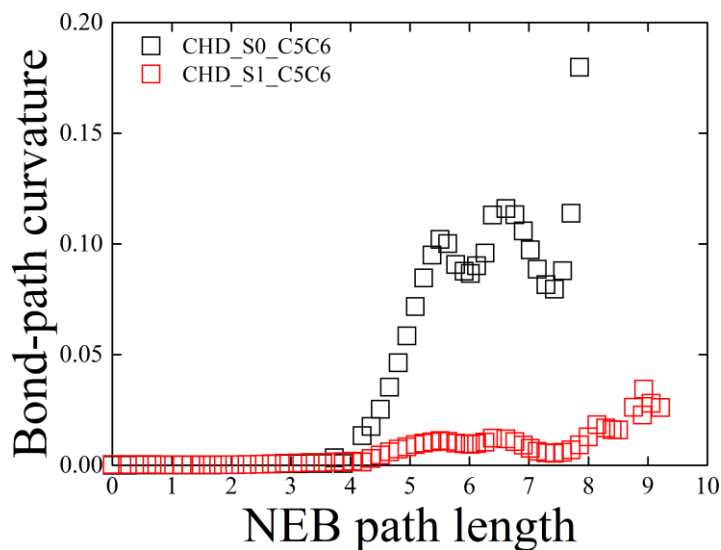
(d)



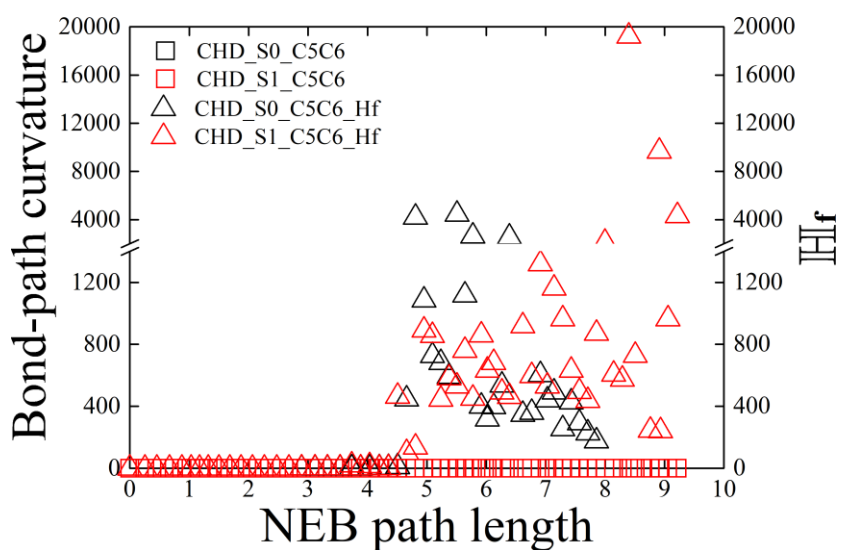
(e)



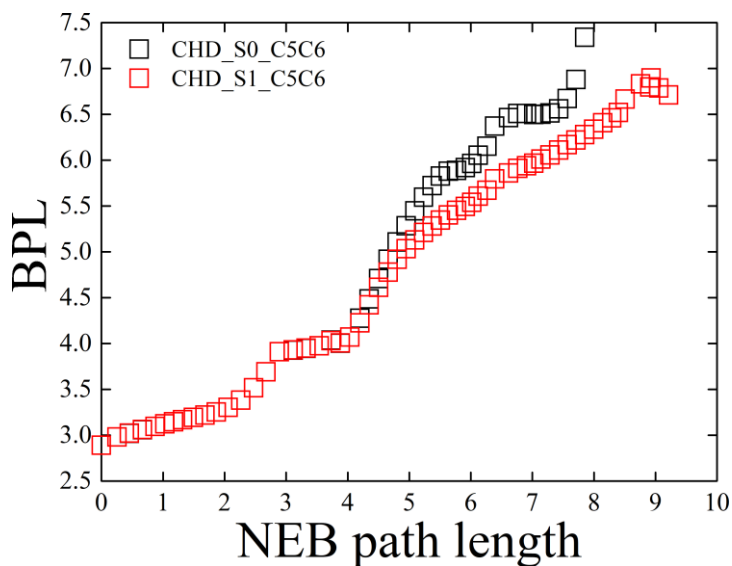
(f)



(g)



(h)



(i)

Figure S3. The eigenvector-following path length \mathbb{H} and the corresponding variations eigenvector-following path length \mathbb{H}^* of the C5-C6 BCP are shown in (a-b) respectively. The eigenvector-following path length \mathbb{H}_f and the corresponding variation the fractional eigenvector-following path length \mathbb{H}_f^* of the C5-C6 BCP are shown in (c-d) respectively. The variation of the $\mathbb{H}_{f0\min} = (\mathbb{H} - \mathbb{H}_{0\min})/\mathbb{H}_{0\min}$ and the corresponding value for $\mathbb{H}_{f0\min}^* = (\mathbb{H}^* - \mathbb{H}_{0\min}^*)/\mathbb{H}_{0\min}^*$ of the C5-C6 BCP are shown in (e-f) respectively. The variation of the bond-path curvature (BPL-GBL)/GBL and corresponding with \mathbb{H}_f of the C5-C6 BCP are shown in (g-h). The variation of the bond-path lengths (BPL) of the C5-C6 BCP is shown in (i).

4. Supplementary Materials S4.

The reasons for the choice of the ellipticity ε as scaling factor. This was motivated by the fact that the scaled vector tip paths drop smoothly onto the bond-path, ensuring that the tip paths are always continuous. We previously discussed the unsuitability of alternative scaling factors, $|\lambda_1 - \lambda_2|$ this was not pursued as it lacks the universal chemical interpretation of the ellipticity ε e.g. double-bond $\varepsilon > 0.25$ vs. single bond character $\varepsilon \approx 0.10$. Also unsuitable choices for scaling factors, on the basis of not attaining zero, included either ratios involving the λ_1 and λ_2 eigenvalue or any inclusion of the λ_3 eigenvalue. The λ_3 eigenvalue was also found to be unsuitable because it contains no information about the least ($\underline{\mathbf{e}}_1$) and most ($\underline{\mathbf{e}}_2$) preferred directions of the total charge density $\rho(\mathbf{r})$ accumulation.

Discussion on the uniqueness of the \mathbb{H}^* and \mathbb{H} . Because \mathbb{H}^* and \mathbb{H} are defined by the distances swept out by the $\underline{\mathbf{e}}_2$ tip path points $\mathbf{p}_i = \mathbf{r}_i + \varepsilon_i \underline{\mathbf{e}}_{1,i}$ and $\mathbf{q}_i = \mathbf{r}_i + \varepsilon_i \underline{\mathbf{e}}_{2,i}$ respectively and the scaling factor, ε_i is identical in equation (3a) and equation (3b) therefore for a linear bond-path \mathbf{r} then $\mathbb{H}^* = \mathbb{H}$. The bond-path framework set $\mathbb{B} = \{\mathbf{p}, \mathbf{q}, \mathbf{r}\}$ should consider the bond-path to comprise the *unique* \mathbf{p} -, \mathbf{q} - and \mathbf{r} -paths, swept out by the $\underline{\mathbf{e}}_1$, $\underline{\mathbf{e}}_2$ and $\underline{\mathbf{e}}_3$, eigenvectors that form the eigenvector-following paths with lengths \mathbb{H}^* , \mathbb{H} and BPL respectively. The \mathbf{p} - and \mathbf{q} -paths are unique even when the lengths of \mathbb{H}^* and \mathbb{H} are the same or very similar because the \mathbf{p} - and \mathbf{q} -paths traverse different regions of space. Bond-paths \mathbf{r} with non-zero bond-path curvature which will result in \mathbb{H}^* and \mathbb{H} with different values, this is more likely to occur for the equilibrium geometries of closed-shell *BCPs* than for shared-shell *BCPs*. This is because the \mathbf{p} - and \mathbf{q} -paths will be different because of the greater distance travelled around the outside of a twisted bond-path \mathbf{r} compared with the inside of the same twisted bond-path \mathbf{r} . This is because within QTAIM the $\underline{\mathbf{e}}_1$, $\underline{\mathbf{e}}_2$ and $\underline{\mathbf{e}}_3$, eigenvectors can only be defined to within a factor of -1, i.e. $(\underline{\mathbf{e}}_1, -\underline{\mathbf{e}}_1)$, $(\underline{\mathbf{e}}_2, -\underline{\mathbf{e}}_2)$ and $(\underline{\mathbf{e}}_3, -\underline{\mathbf{e}}_3)$ therefore there will be two possible tip-paths. The consequences of this (within QTAIM) calculation of the \mathbb{H}^* is that we dynamically update the sign convention to define \mathbb{H}^* as being the shorter of the two possible tip-paths because $\underline{\mathbf{e}}_1$ is the least preferred direction of accumulation of $\rho(\mathbf{r})$. A similar procedure is used for \mathbb{H} except that we chose the longer of the two possible tip-paths because $\underline{\mathbf{e}}_2$ is the most preferred direction of accumulation of $\rho(\mathbf{r})$.

Implementation details of the calculation of the eigenvector-following path lengths \mathbb{H} and \mathbb{H}^* .

When the QTAIM eigenvectors of the Hessian of the charge density $\rho(\mathbf{r})$ are evaluated at points along the bond-path, this is done by requesting them via a spawned process which runs the selected underlying QTAIM code, which then passes the results back to the analysis code. For some datasets, it occurs that, as this evaluation considers one point after another in sequence along the bond-path, the returned calculated $\underline{\mathbf{e}}_2$ (correspondingly $\underline{\mathbf{e}}_1$ is used to obtain \mathbb{H}^*) eigenvectors can experience a 180-degree ‘flip’ at the ‘current’

bond-path point compared with those evaluated at both the ‘previous’ and ‘next’ bond-path points in the sequence. These ‘flipped’ $\underline{\mathbf{e}}_2$ (or $\underline{\mathbf{e}}_1$) eigenvectors, caused by the underlying details of the numerical implementation in the code that computed them, are perfectly valid, as these are defined to within a scale factor of -1 (i.e. inversion). The analysis code used in this work detects and re-inverts such temporary ‘flips’ in the $\underline{\mathbf{e}}_2$ (or $\underline{\mathbf{e}}_1$) eigenvectors to maintain consistency with the calculated $\underline{\mathbf{e}}_2$ (or $\underline{\mathbf{e}}_1$) eigenvectors at neighboring bond-path points, in the evaluation of eigenvector-following path lengths \mathbb{H} and \mathbb{H}^* .

5. Supplementary Materials S5.

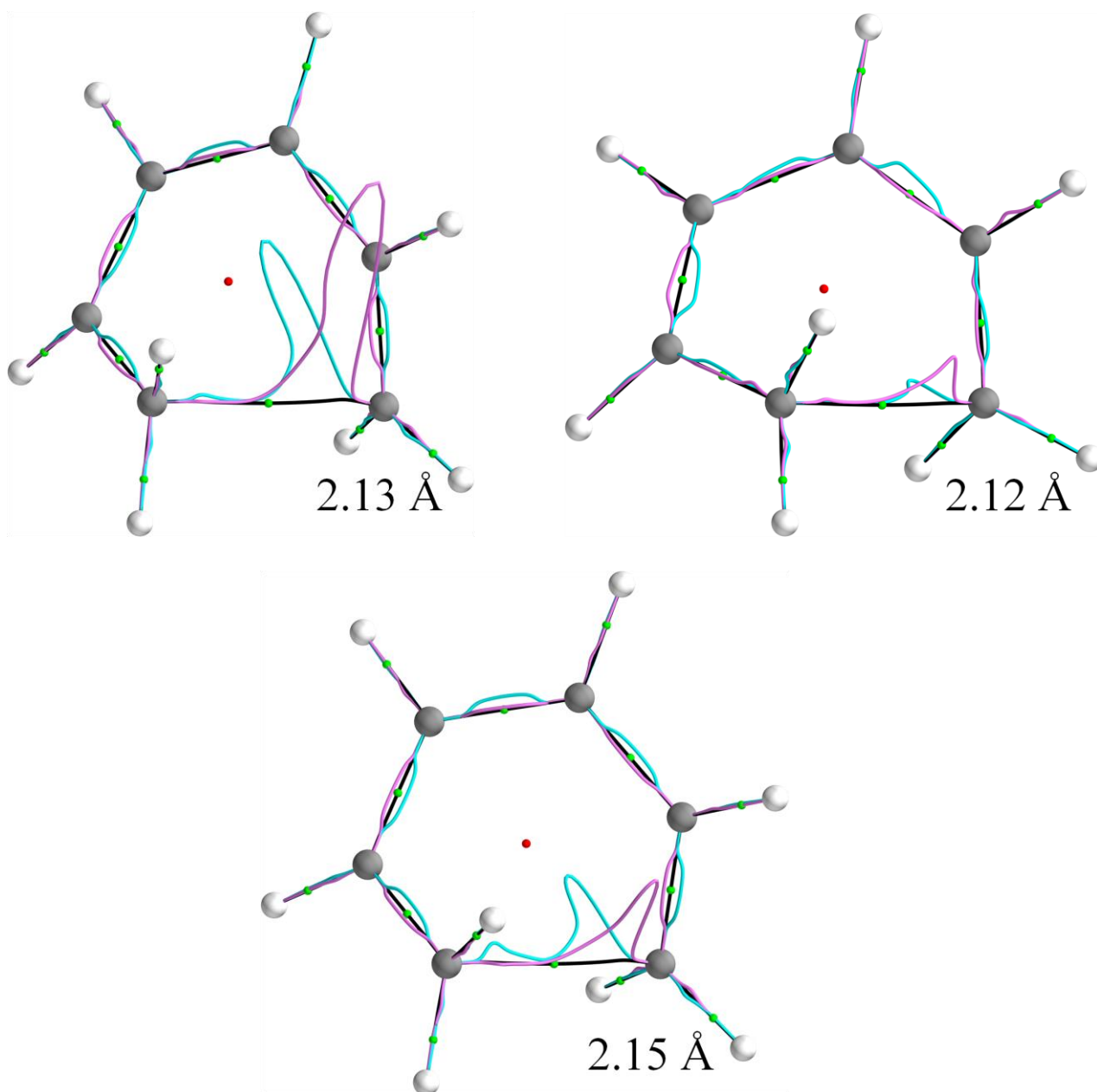


Figure S5. The values of $\mathbb{B} = \{(p_0, q_0), r\}$ corresponding to the S_0 state of the CHD \rightarrow HT photoreaction for values of $R(\text{C5-C6}) = 2.13 \text{ \AA}$, 2.12 \AA and 2.15 \AA are presented in sub-figures (a)-(c) respectively. Note that these values of $R(\text{C5-C6})$ correspond to the closed-shell C5--C6 *BCP*, shared-shell C5-C6 *BCP* and closed-shell C5--C6 *BCP* bond-path in sub-figures (a)-(c) respectively.